

January 1988

Measured and Calculated Acoustic Attenuation Rates of Tuned Resonator Arrays for Two Surface Impedance Distribution Models With Flow

Tony L. Parrott,
A. Louis Abrahamson,
and Michael G. Jones

(NASA-TP-2766) MEASURED AND CALCULATED
ACOUSTIC ATTENUATION RATES OF TUNED
RESONATOR ARRAYS FOR TWO SURFACE IMPEDANCE
DISTRIBUTION MODELS WITH FLOW (NASA) 51 p

N88-17440

CSCL 20A H1/71

Unclas
0103620

1988

Measured and Calculated
Acoustic Attenuation
Rates of Tuned Resonator
Arrays for Two Surface
Impedance Distribution
Models With Flow

Tony L. Parrott
Langley Research Center
Hampton, Virginia

A. Louis Abrahamson
COMTEK
Grafton, Virginia

Michael G. Jones
PRC Kentron, Inc.
Hampton, Virginia



National Aeronautics
and Space Administration

Scientific and Technical
Information Division

Contents

Summary	1
Symbols	1
Introduction	2
Experimental Setup and Measurement Procedures	3
Test Models	3
Resonator Normal Incidence Impedance Measurements	3
Resonator Flow Resistance Measurements	4
Flow Impedance Tube	4
Acoustic Measurements in Flow Impedance Tube	5
Analysis	6
Requirements and Approximations	6
Two-Dimensional Modal Decomposition Model	6
Smeared impedance method	6
Equivalent length method	6
Formulation of two-dimensional modal decomposition method	7
Two-Dimensional Finite Element Model	7
Two-Microphone Intensity Measurement Technique	9
Results and Discussion	9
Impedance Measurements	9
Broadband Acoustic Attenuation Measurements	10
Measured and Calculated Axial Attenuation Profiles	10
Measured and Calculated Transmission Losses	12
Effects of Mean Flow on Resonator Array Attenuation	13
Concluding Remarks	14
References	14
Figures	16

PRECEDING PAGE BLANK NOT FILMED

Summary

The objective of this investigation was to validate two propagation models (modal decomposition and finite element) for predicting the performance at low frequencies of duct liner configurations built up from an array of seven individually tuned resonators. Most tests were conducted on a configuration consisting of round resonator cavities. However, limited tests were also conducted on a configuration with square resonator cavities. These analytical models had previously been developed for high frequency attenuation in aero-engine inlets, but no satisfactory validation of their accuracy existed in the low frequency range. In the low frequency application, the liner surface impedance is characterized by spatial variations as a consequence of available structural components and fabrication techniques. The scale of these variations may cause the liner to appear acoustically nonuniform.

The modal decomposition model was of the "infinite waveguide" type and consequently assumed a uniform surface impedance distribution. The finite element model, on the other hand, could handle surface impedance nonuniformities in the axial direction but assumed uniformity in the transverse direction. Thus, to provide acceptable impedance boundary conditions for the two predictive models, two procedures were used to modify the impedance distributions. A "smeared" impedance distribution removed spatial nonuniformities by equating volume velocities between the resonator active area and its respective apportioned area in the array. This procedure resulted in a specific impedance change. An "equivalent length" impedance distribution procedure simply distorted the active circular area of each resonator into an equivalent length, such that the specific impedance was preserved. For the modal decomposition model, both procedures were applied to provide a uniform surface impedance free of transverse and axial dependence. The equivalent length distribution procedure was used to remove only the transverse impedance variation so that a two-dimensional finite element propagation model could be implemented with axial impedance variations left intact.

Attenuation rates predicted with the modal decomposition propagation model were generally in good agreement with measured attenuation rates, for the round and square resonator arrays. This was true for both impedance distribution modeling procedures and for frequencies up through the first resonance of the resonator backing cavities, or for nondimensional frequency parameter kh values of 0.8. Attenuation rates obtained from the finite element

model were in excellent agreement with the measured values, as were the attenuation profiles. For the square resonator array, the predicted and measured attenuation profiles did not agree as well, although the attenuation rates were still in very good agreement.

Predicted and measured transmission losses for test frequencies beyond the resonator cavity first resonance were in very good agreement when all resonator cavity depths were set the same. For linearly varying cavity depths, predicted and measured transmission loss trends were still in good agreement, but less so than for uniform cavity depths.

Detailed calculations of attenuation and phase profiles, at axial locations near the resonator array elements and in the presence of mean flow, revealed a fine-scale structure of acoustic "hot spots" superimposed on the general acoustic field structure. Careful measurements verified the existence of such hot spots, which apparently are attributable to convective effects alone, since no flow-induced impedance changes were assumed in the model.

Symbols

A	amplitude coefficient
A_{mn}, B_{mn}	amplitude coefficients associated with the m th acoustic mode
c	sound speed
dB_h	attenuation per duct height, in dB
D	single resonator diameter
h	duct height
i	$= \sqrt{-1}$
I	acoustic intensity
I_i	incident acoustic intensity
I_t	transmitted acoustic intensity
$[J]$	Jacobian matrix
k	free-space acoustic wave number, ω/c
kh	nondimensional frequency parameter or nondimensional duct size
k_{mn}	total wave number associated with the m th acoustic mode
l	typical duct dimension
L	single resonator length

L_e	axial dimension	z	distance across duct in horizontal direction
m, n	spinning wave numbers	Z	resonator acoustic impedance
M	centerline Mach number	Z_E	equivalent acoustic impedance
N_1, N_2, N_3, N_4	finite element shape functions	Z_s	smearred acoustic impedance
$p(x, y, z)$	acoustic pressure	α_n	wave number in z -direction
p_A	acoustic pressure at leading edge	$\beta_1, \beta_2, \beta_3, \beta_4$	wall admittances
p_B	acoustic pressure at trailing edge	γ_m	wave number in y -direction
p_s	static pressure	ζ	acoustic impedance, normalized by ρc
p_t	total pressure	η, ξ	set of local coordinates within the region
P_{12}	pressure ratio, $\frac{p(x_1)}{p(x_2)}$	ρ	density
Q	constant (see eq. (7))	$\bar{\rho}$	mean density
r	duct radius	ω	source frequency
r_i, x_i	global coordinates of corner nodes	∇	Laplace operator
R	reflection coefficient	Abbreviations:	
Re	Reynolds number	LE	leading edge
R_f	flow resistance	SPL	sound pressure level
t	time, $e^{-i\omega t}$ time convention assumed	TE	trailing edge
T	temperature, °C	Introduction	
u, v, w	acoustic particle velocities in x -, y -, and z -directions, respectively	The efficient suppression of unwanted sound in ducted air-moving systems is of continuing interest for numerous applications. Although silencer technology is very advanced for many applications (such as automotive exhaust mufflers and turbojet engine inlets), new and unique requirements continue to make severe demands on current technology. One such requirement arises from the urgent need for ultraquiet wind tunnels for specialized aerodynamic tests, such as the investigation of transition from laminar to turbulent flow in the absence of acoustic excitation. The receptivity of laminar flow to acoustic excitation is of particular interest, since it may be a barrier to obtaining the significant drag reduction associated with laminar flow (see refs. 1, 2, 3, and 4).	
u_1, u_2, u_3, u_4	values of u, v, w , or p at the four node points at the numbered corners of the element	Abrahamson (ref. 5) proposed an ultraquiet wind-tunnel design for laminar flow transition research which set an acoustic noise level limit not to exceed 60 dB in any octave band from 31 to 4000 Hz. Such a requirement is particularly difficult to meet at low frequencies because of turbulent processes such as aerodynamic throttling, interaction with vibrating panels, and flow turning. One way to obtain	
v^*	complex conjugate of acoustic velocity		
W	resonator width		
x	distance measured along duct axis		
x_1, x_2	axial positions		
y	height above lower wall of duct (resonator array surface)		
$Y_m(y), Z_n(z)$	eigenfunctions		

greater attenuations at low frequencies is to integrate individually tuned resonator absorbers into a "smooth" wall diffuser. Thus, the sound absorbing walls must be aerodynamically smooth and conform to the desired streamline flow pattern to minimize self-noise and to maintain flow quality. Traditional automotive-type, low frequency resonator muffler technology, which incorporates flow direction changes and flow path discontinuities to attenuate exhaust noise, is unacceptable for these stringent requirements.

The development of resonant liner technology was greatly stimulated in the early 1970's by the introduction of the turbofan engine into the civilian airline fleet. An intense research effort was directed toward reducing high frequency noise (2.5 kHz to about 10 kHz) radiating through turbofan inlet ducts to the environment. Partly because of size, weight, and performance advantages, resonant duct liners with relatively smooth surfaces were the predominant choice for duct liner acoustic treatments. Lawson, in reference 6, gives an overview of duct liner technology with emphasis on application to aero-engine ducts. Similarities between the geometry of the aero-engine duct and that of the present application suggest the applicability of the same technology, but at wavelength scales 10 to 100 times larger.

The purpose of this paper is to describe a scale model, experimental validation of two theoretical techniques available for use in low-frequency-attenuating duct liner applications. One aspect to be investigated was the surface impedance distribution modeling procedure for specifying the boundary conditions to achieve acoustic attenuation rates predicted by these techniques. To this end, two different scale model resonator arrays were fabricated, and their acoustic performances were measured and compared with analytical predictions using both a closed form modal approach and a finite element analysis. The following sections of this report describe comparisons between the two theoretical models on the basis of calculated and measured axial attenuation rates, attenuation and phase profiles, and transmissions losses for a scale model, linear array of resonators. Individual resonators consisted of round backing cavities fitted with movable pistons for variable tuning. The resistive element was provided by a porous fiber metal screen bonded to the resonator openings. The resulting resonator array was thus characterized by circular regions of relatively low impedance separated by regions of "hard wall." Limited tests were also conducted on a resonator array with square backing cavity cross sections, in which case the hard wall interstitial regions between resonators were considerably

reduced compared with those for the round resonator array.

Experimental Setup and Measurement Procedures

Test Models

Figures 1 and 2 show sketches of the round and square cavity resonator array test models, respectively. The structure of the round cavity resonator array of figure 1 will be discussed in detail. The same remarks also apply to the square cavity resonator array, except for the obvious geometrical difference. The seven resonator cavities were fabricated from 1.75-in-id aluminum tubing with a wall thickness of 0.125 in. To form a linear array of seven resonators, the cylindrical cavities (round or square) were set into an epoxy fixture as shown in the figure. Cavity depths were adjustable from 0 to 5.4 in. by means of adjustable pistons equipped with O-ring seals. It should be noted from the figures that the overall axial length and width of both resonator arrays were 15.5 in. and 2.0 in., respectively. Thus, each resonator could be apportioned an axial length of 2.2 in. The resistive component of the resonator impedance was supplied by a porous fiber metal face sheet of thickness 0.028 in., with a nominally rated flow resistance of 100 kg/m²-sec. A single strip of this fiber metal, with dimensions 15.5 in. × 2.0 in., was removed from a parent sheet and bonded to the epoxy fixture. Thus, the resistive elements for each resonator consisted of circular regions of the face sheet congruent with the resonator mouth.

Figures 3(a) and (b) show photographs of the two completed resonator arrays. Figure 3(a) shows a view of the arrays from the front, or active, side, and figure 3(b) shows a view of the backing cavities with a few of the airtight, adjustable pistons inserted. The square cavity resonator array is shown attached to the fixture that allows the resonator array to be installed on the bottom wall of the flow impedance tube apparatus. Note that in figure 3(a) there appears to be some "wicking" of the bonding agent into the resonator mouth areas. This effect appears most pronounced for the square resonator array. However, visual inspection, by observing differences in light transmission through the face sheet over the resonator mouth areas, indicated that the square resonator active face-sheet areas were evidently more uniform than those of the round resonator array.

Resonator Normal Incidence Impedance Measurements

Although the contribution of the resonator cavity reactive component to the total impedance can be

reliably calculated, such is not the case for the resistive face-sheet contribution. The manufacturer's nominal flow resistance value is merely a selection guide and may be subject to a variance of up to 25 percent from sample to sample. Thus, to ascertain a more accurate estimate of the acoustic impedance, the normal incidence impedance was measured for a typical resonator from each resonator array and flow resistance measurements were conducted on all the resonator resistive face sheets.

Normal incidence impedance data were obtained by means of the two-microphone method, implemented with one of two "impedance tubes" (one of which is shown in fig. 4). These impedance tubes were constructed of 1-ft lengths of the same cylindrical tubing used for the resonator array cavities, thereby avoiding area discontinuities between the impedance tube and the active resonator area. Handles were attached to hold the device in place against the resonator whose impedance was to be measured. A seal between the tube and the resonator face was provided by a rubber gasket, as shown in the photograph.

Instrumentation for the two-microphone impedance measurement method is shown in figure 5. Acoustic plane waves in the frequency range 0.5 to 3.0 kHz were propagated down the tube and were normally incident on one of the seven resonator array elements, which was aligned and pressed against the gasketed, open end of the impedance tube. The amplitude and phase for each frequency of interest were measured at two probe ports located 2.08 in. and 3.08 in. from the face of the test specimen. The microphones used in this measurement were $\frac{1}{2}$ -in. condenser microphones connected to $\frac{1}{16}$ -in.-id stainless steel probe tubes, with lengths such that the ends were flush with the impedance tube inside wall. Amplitude and phase data were acquired by way of the signal path illustrated at the left of the diagram. This data acquisition system was essentially the same as that used to acquire the axial attenuation and phase profiles and will be described in more detail in the "Acoustic Measurements in Flow Impedance Tube" section. To ensure constant levels at the resonator face during impedance measurements, signals from a $\frac{1}{4}$ -in. reference microphone, located adjacent to the resonator face, were input to a feedback loop (automatic level regulator).

Resonator Flow Resistance Measurements

The dc flow resistance of a thin porous material is defined as the pressure drop across the material per unit incident steady flow velocity. It is a useful indicator of the acoustic resistance if the

test specimen is thin compared with the relevant acoustic wavelengths and if flow velocities are not too high compared with the acoustic particle velocities of interest. To conveniently measure and evaluate the variability of the acoustic resistance values of all the resonators, a computer-controlled valve and flowmeter arrangement was used to measure the flow resistance of each resonator. To accomplish this measurement, steady airflow was forced through the face of each resonator, by way of the backing cavities, at a series of precisely controlled velocities. The principle of operation of such an apparatus is described in reference 7. Corresponding pressure drops and flow velocities across the resistive face sheet of each resonator were measured and used to compute the flow resistance. Clearly, flow resistance is far more convenient to measure than acoustic impedance. Thus, in this investigation, flow resistance measurements were used to determine the acoustic resistance variations among the resonators.

Flow Impedance Tube

In this experiment, several different acoustic tests were performed on the resonator arrays to ascertain their acoustic characteristics in a grazing incidence and/or grazing flow environment. The tests were conducted in the flow impedance test apparatus at the Langley Research Center, as shown in figure 6 (ref. 7). This multiconfigurational apparatus is designed to produce a controlled aeroacoustic environment with sound pressure levels up to 140 dB and a flow speed of up to Mach 0.6, over a test specimen length up to 15.5 in. Moving from left to right in the figure, it is convenient to divide the apparatus into three sections as indicated. The source section begins with a supply plenum from which air (if flow is desired) percolates into a 2.25-in.-diameter round duct constructed of high-resistance fiber metal. A thermocouple located at the plenum exit provides a control point for airflow temperature, and a pitot-static tube located about 12 duct diameters downstream from the plenum exit provides a means for determining a reference centerline Mach number. An electromagnetic, 120-W acoustic driver is used to propagate either broadband or pure tone plane waves through the square cross section (2 in. \times 2 in.) of the test section region. The acoustic waves are gradually combined with the flow through the high-resistance (60 000 kg/m²-sec) cylindrical duct as shown. Cross-section areas are maintained constant throughout the system. Also, over a region from 5 in. upstream of the test linear leading edge (LE) to 2 in. downstream of the test linear trailing edge (TE), axially uniform flow conditions can be maintained.

Over the test specimen region (indicated by LE and TE in the figure), and 48 in. upstream of it, a 0.5-in.-wide precision-machined slot in the top wall allows an axial bar to traverse the test section length by means of a digital stepping motor under computer control. The traversing bar will accommodate the installation of several different types of transducers. In this experiment, measurements were made with either a flush-mounted condenser microphone or a strain gauge pressure sensor incorporated into a specially designed, streamlined probe, as described in reference 8. Under control of data acquisition programs, these sensors could sample the acoustic field at desired locations. These data provided the attenuation and phase profiles over the test specimen length (as suggested by the sketch beneath the test specimen location) and information for calculating acoustic intensities upstream of the leading edge and downstream of the trailing edge.

Test specimen lengths up to 15.5 in. can be accommodated in the bottom wall of the test section. With the full length of the test specimen installed, a transducer mounted on the traversing bar can probe the entire length of the test specimen, plus about 48 in. upstream of the test specimen leading edge and at least 2 in. downstream of the trailing edge. In this manner, the acoustic wave fields upstream and downstream of the test specimen can also be measured. A more detailed description of this axial-traversing measurement system is given in reference 8. For some tests, total attenuations across the resonator array were obtained with $\frac{1}{4}$ -in. condenser microphones flush-mounted in the side walls of the tube at the leading and trailing edges.

Acoustic waves exiting the test section region are absorbed by an anechoic termination section specially designed to be nonreflective with or without mean flow present. This section consists of a 20-ft-long 2-in. \times 2-in. duct, with the two absorptive vertical walls consisting of a 30-percent perforated plate backed by open-celled foam compressed to one-seventh the original volume at the entrance end of the termination. The compression gradually decreases over the 20-ft termination length. A 2-ft foam wedge is encountered near the termination end, as shown in figure 6. This design was intended to inhibit flow noise and to allow the acoustic waves to be absorbed without significant reflection back into the test section region.

Airflow through the flow impedance tube was provided by the combination of a pressurized plenum in the source section and a vacuum source at the exit of the termination section. An automatic electromechanical control system maintained constant flow through the test section to within about

3 percent of a preset Mach number. Static pressure at the leading edge of the test section was maintained to within about ± 3 mm Hg of a preset value, and the free-stream static temperature of the airflow was maintained to within $\pm 2^\circ\text{C}$ of a preset value by means of electric heaters in the air supply line. From experience, flow stability was optimum when the static pressure at the test section was maintained 5 to 10 mm Hg below local barometric pressure and the static temperature was maintained at ambient temperature.

Acoustic Measurements in Flow Impedance Tube

Acoustic tests conducted in the flow impedance tube apparatus consisted of broadband attenuation measurements, axial attenuation and phase profile measurements for pure tones, and transmission loss measurements. The instrumentation for accomplishing these measurements is depicted in figure 7. Depending on whether a pure tone or broadband excitation was desired, the power amplifier was driven by a programmable frequency synthesizer or a random noise generator. To obtain the broadband attenuation measurements across the resonator array, the transfer function magnitude was measured between the microphones located at the leading and trailing edges by means of the spectrum analyzer shown at the right of the diagram. To obtain the pure tone axial attenuation and phase profiles, the signal processing path for the pressure probe signal shown at the center of the diagram was used. After appropriate signal conditioning, the signal was filtered through a 50-Hz bandwidth tracking filter to remove harmonics of the signal generated by the acoustic driver, which was operated near its peak capacity. To further improve the dynamic range of the measurement process, the signal was then subjected to synchronous averaging to remove residual random noise. This step was really only necessary with flow, but was also included in the no-flow measurements for consistency. Absolute sound pressure level and phase were then calculated with the computer by using stored calibration information. These calculated values were also stored for later use to generate axial attenuation and phase plots.

Transmission losses were obtained by determining acoustic intensities I_i and I_t associated with the incident and transmitted plane waves in the hard-wall regions of the test section upstream and downstream of the test specimen leading and trailing edges. At the leading and trailing edges of the resonator array, the plane wave is necessarily contaminated by higher order modes to provide continuity of the acoustic field across the discontinuity between the hard and

soft walls. These higher order modes are below their cut-on frequencies, however, and tend to attenuate rapidly with distance from the discontinuity. Thus, to obtain valid measurements of transmission loss for the plane wave, the acoustic intensities should be obtained at sufficient distances from the leading and trailing edges to ensure that higher order modes have decayed. Experimentally, this will be the case if the intensity measurements are location independent.

The intensity measurement procedure, from which transmission losses, $10\log(I_i/I_t)$, were obtained, is described in the "Analysis" section and can be treated as a modification of the two-microphone impedance measurement method. In the present situation, the computer-controlled microphone positioning capability allowed a single microphone, flush mounted on the traversing bar, to replace the two microphones normally used in the two-microphone method. In this manner the need for accurate, and tedious, microphone calibrations was eliminated. Measurements were made 10.0 in. and 9.0 in. upstream of the liner leading edge, and 2.0 in. and 1.0 in. downstream of the liner trailing edge. The data acquisition was done in a manner almost identical to that used in the normal incidence impedance measurements. Since the results were not position dependent, direct comparisons between the predicted and measured transmission losses could then be made.

Analysis

Requirements and Approximations

It is well known that acoustic propagation phenomena through lined ducts scale on the dimensionless parameter kh , where $k = \omega/c$ and h is a typical duct dimension. This fact permits propagation model validation experiments performed over one frequency range to be applicable to another frequency range. The test results presented in this paper were obtained over a kh range of 0.3 to 2.5 (0.3 to 3.0 kHz), where h is the duct height.

A rigorous, analytical treatment of sound propagation in a muffler that is also designed to double as a diffuser and that incorporates individually tunable resonators distributed over the walls, would require a fully three-dimensional (3-D) analytical model. The importance of 3-D effects, however, depends on many factors, including acoustic source frequency, duct geometry and its rate of change with axial distance, and acoustic wall impedance distribution. Since no modeling code was available that would fully incorporate all possible 3-D effects, two separate codes were used which employed different sets of simplifying assumptions. The results of both analyses were then

compared to provide a cross-check on these assumptions. These codes were the modal analysis code developed by Watson (refs. 9, 10, and 11), and the finite element code ADAM (refs. 12 and 13). A brief description of the two methods follows.

Two-Dimensional Modal Decomposition Model

The disadvantage of the Watson formulation is that it is unable to handle the effects of axial variations either of duct geometry or of duct liner impedance. Thus, it was necessary to employ an "equivalent" axially uniform impedance to approximate the impedance distribution. Two different methods of deriving this equivalent impedance were used. In an a priori sense, either of these methods is equally acceptable, since they both employ an assumption to smooth out the nonuniformities present in the surface impedance distribution. These two methods for deriving the equivalent impedance distribution will be described with the aid of figure 8. Figure 8(a) depicts the actual geometry of the resonator array impedance distribution drawn to scale. The circular shaded areas of diameter D represent the resonator impedances Z . It should also be noted that exactly the same procedure was used for the round and square resonator arrays.

Smeared impedance method. In this modeling procedure, each resonator impedance was uniformly distributed over its apportioned length L and width W in the array, as suggested in figure 8(b). Physically, this means that acoustic volume flows through the actual and idealized resonator face sheets are equated. Thus, the specific acoustic impedance is different for the idealized resonator face sheet by the ratio of the so-called smearing factor. The smearing factor on the measured impedance was 1.83 for the round resonator array and 1.44 for the square resonator array. Both the smeared and equivalent length (to be described next) impedance distribution models were used with the two-dimensional (2-D) modal decomposition propagation model.

Equivalent length method. With reference to figure 8(c), the circular area of a single resonator of diameter D in the array is equated to an equivalent rectangular area with axial dimension L_e and width W . Thus, for the circular resonator diameter of 1.75 in., the resultant equivalent length is 1.2 in. This equivalent length corresponds to about 55 percent of the apportioned length of 2.2 in. for each resonator element and therefore for the entire resonator array length. Note that this modeling procedure conserves specific acoustic impedance, since it only changes the shape of the impedance region. Figure 8(d)

shows the equivalent length procedure as applied in modeling the array impedance distribution for the finite element code to be described later in this section. The advantage of this code is the ability to account for axial variations in impedance.

Formulation of two-dimensional modal decomposition method. The formulation of the 2-D modal decomposition method is based on a closed-form solution to the Helmholtz equation in a rectangular duct by separation of variables. In the absence of mean flow, acoustic waves propagating in a duct (fig. 9(a)) are governed by the 3-D Helmholtz equation

$$\nabla^2 p + k^2 p = 0 \quad \left(k = \frac{\omega}{c}\right) \quad (1)$$

A harmonic solution in x is of the form

$$p(x, y, z) = \sum_{m=1}^{\infty} \sum_{n=1}^{\infty} (A_{mn} e^{ik_{mn}x} + B_{mn} e^{-ik_{mn}x}) Y_m(y) Z_n(z) \quad (2)$$

where the eigenfunctions Y_m and Z_n must satisfy the boundary conditions

$$\frac{\partial Y_m}{\partial y} - ik\beta_4 Y_m = 0 \quad (\text{at } y = h) \quad (3)$$

$$\frac{\partial Y_m}{\partial y} + ik\beta_3 Y_m = 0 \quad (\text{at } y = 0) \quad (4)$$

$$\frac{\partial Z_n}{\partial z} - ik\beta_2 Z_n = 0 \quad (\text{at } z = 1) \quad (5)$$

$$\frac{\partial Z_n}{\partial z} + ik\beta_1 Z_n = 0 \quad (\text{at } z = 0) \quad (6)$$

(Wall admittances β are shown in fig. 9(a).) Suppose a solution for Y_m of the form

$$Y_m = \cos \gamma_m y + Q \sin \gamma_m y \quad (7)$$

then

$$\frac{\partial Y_m}{\partial y} = -\gamma_m \sin \gamma_m y + \gamma_m Q \cos \gamma_m y$$

or, substituting in equation (4)

$$\tan \gamma_m y + \frac{\gamma_m Q + ik\beta_3}{-\gamma_m + ik\beta_3 Q} = 0$$

Now, when $y = 0$, $\tan \gamma_m y = 0$, and thus

$$\gamma_m Q + ik\beta_3 = 0$$

Therefore,

$$Q = \frac{-ik\beta_3}{\gamma_m}$$

and,

$$Y_m = \cos \gamma_m y - \frac{ik\beta_3}{\gamma_m} \sin \gamma_m y \quad (8)$$

Similarly, at $z = 0$ for Z_n , equation (6) gives

$$Z_n = \cos \alpha_n z - \frac{ik\beta_1}{\alpha_n} \sin \alpha_n z \quad (9)$$

Substituting these expressions in equations (3) and (5) we get the transcendental equations

$$(\gamma_m^2 + k^2 \beta_3 \beta_4) \sin \gamma_m h + ik(\beta_3 + \beta_4) \gamma_m \cos \gamma_m y = 0 \quad (10)$$

$$(\alpha_n^2 + k^2 \beta_1 \beta_2) \sin \alpha_n l + ik(\beta_1 + \beta_2) \alpha_n \cos \alpha_n z = 0 \quad (11)$$

Substituting for p in equation (1) gives the eigenvalues

$$k_{mn}^2 = k^2 - \gamma_m^2 - \alpha_n^2 \quad (12)$$

The imaginary part of k_{mn} gives the decay rate in the x -direction for the m th mode. Note that $\gamma_m = \alpha_n = 0$ is always a solution to equations (10) and (11), but this solution gives the additional conditions that

$$k^2 \beta_3 \beta_4 + ik(\beta_3 + \beta_4) = 0 \quad (13)$$

and

$$k^2 \beta_1 \beta_2 + ik(\beta_1 + \beta_2) = 0 \quad (14)$$

Thus, for this trivial case, either $k = 0$ or $\beta_1 = \beta_2 = \beta_3 = \beta_4 = 0$. The latter instance represents a plane wave solution for a hard-wall duct.

A general solution of equations (10) through (12) is only possible numerically, for example, by using a Newton-Raphson scheme (ref. 14). An alternate procedure that was used in this study was to use a one-dimensional (1-D) finite element formulation of a 2-D representation of equation (1) in the x - y plane together with boundary condition equations (3) and (4) to obtain eigenvalues γ_m . A similar 1-D finite element formulation of a 2-D representation of equation (1) in the x - z plane together with boundary condition equations (5) and (6) gives α_n . The combined eigenvalues k_{mn} are then synthesized, as before, with equation (12). This procedure was suggested by Watson (ref. 11).

Two-Dimensional Finite Element Model

A 2-D direct solution method for asymmetric ducts that need not be uniform in the axial direction is described in references 12 and 15. The advantage of this formulation is that it is able to model the effects of duct liner impedance that vary in the axial direction. For the resonator arrays used in the present series of tests, this enabled the axially varying impedance to be modeled as shown in figure 8(d). Here the impedance and equivalent surface area of each resonator is modeled separately with the equivalent length method, as was done for the modal analysis code for the entire resonator array.

The disadvantage of the particular finite element model used in this investigation is that it is necessary to assume some dependence of acoustic variables in the transverse direction. Usually, for a square-section duct such an assumption is not valid unless the solutions for many cross-modes are summed. In this case, however, both side walls are hard and only the plane wave mode is cut on, so that the plane wave assumption that all acoustic variables are independent of transverse direction is valid in sections of the duct where the upper and lower walls are also hard. In the duct section containing the resonators, some transverse dependence does exist, however. This is especially true for the round resonators, since the transverse impedance varies because of the resonator shape. It was anticipated that the tests described in this report would determine the accuracy of these simplifying assumptions.

The finite element scheme employed for this analysis was comprised of a matrix of 20×150 elements, and is fully described in reference 13. There the full theoretical scheme for the numerical solution for sound propagation in a compressible flow is outlined. For simplicity, this analysis is summarized here without the effects of flow.

The four equations governing the linearized acoustic motion in a nonuniform axisymmetric duct are

$$\omega u + \frac{1}{\bar{\rho}} \frac{\partial p}{\partial x} = 0 \quad (15)$$

$$\omega v + \frac{1}{\bar{\rho}} \frac{\partial p}{\partial r} = 0 \quad (16)$$

$$\omega w + \frac{m}{\bar{\rho} r} p = 0 \quad (17)$$

$$\frac{\omega p}{c^2} + \bar{\rho} \left(\frac{\partial u}{\partial x} + \frac{\partial v}{\partial r} + \frac{m}{r} w + \frac{v}{r} \right) = 0 \quad (18)$$

where u, v, w are the acoustic particle velocities, p is the acoustic pressure, $\bar{\rho}$ is the mean density, m is the spinning wave number, c is the speed of sound, and ω is the source frequency. The cylindrical coordinate

system of this formulation can be used to model a rectangular duct with only a plane wave cut on by making $m = 0$ and r equal to a large number (approximating to y in fig. 9(b)), so that $w = 0$ (i.e., plane wave propagating in a large annular duct with annulus height much less than duct radius).

Suppose that within a rectangular element (see fig. 9(b)) the acoustic particle velocities u, v , and the acoustic pressure p are defined by relations of the following type:

$$u = (N_1, N_2, N_3, N_4) \begin{Bmatrix} u_1 \\ u_2 \\ u_3 \\ u_4 \end{Bmatrix} = (N)\{u\} \quad (19)$$

where u_1, u_2, u_3, u_4 are the values of u, v , or p at the four node points at the numbered corners of the element, and (N) are the finite element shape functions.

Define a set of local coordinates (η, ξ) within the region such that the coordinates of the nodes (η_i, ξ_i) are given by $(-1, -1), (+1, -1), (+1, +1), (-1, +1)$ for $i = 1$ through 4, respectively. The N_i 's of equation (19) are shape functions for a linear Serendipity element and are defined by

$$N_i = \frac{1}{2}(1 + \xi \xi_i)(1 + \eta \eta_i) \quad (20)$$

When the simple rectangular element is mapped to global (r, x) coordinates it may be distorted to fit the required geometry of the problem by the transformation

$$r = (N_1, N_2, N_3, N_4) \begin{Bmatrix} r_1 \\ r_2 \\ r_3 \\ r_4 \end{Bmatrix} = (N)\{r\}$$

$$x = (N_1, N_2, N_3, N_4) \begin{Bmatrix} x_1 \\ x_2 \\ x_3 \\ x_4 \end{Bmatrix} = (N)\{x\} \quad (21)$$

where $(r_1, x_1), (r_2, x_2) \dots$ are the global coordinates of the corner nodes. The spatial derivative of equations (15), (16), (17), and (18) may be expressed in local coordinates by

$$\begin{Bmatrix} \frac{\partial}{\partial r}(N) \\ \frac{\partial}{\partial x}(N) \end{Bmatrix} = [J]^{-1} \begin{Bmatrix} \frac{\partial}{\partial \eta}(N) \\ \frac{\partial}{\partial \xi}(N) \end{Bmatrix}$$

where $[J]$ is the Jacobian matrix.

Using the Galerkin version of the method of weighted residuals, we integrate equations (15), (16),

(17), and (18) over the element, weighting each equation in turn by each of the N_i 's to obtain the matrix equations in the nodal variables (ref. 15). It is convenient in integrating these equations to do so in the local, rather than in the global, coordinate system because this greatly simplifies the process because of the convenient limits of integration. Effectively, integration is then over a simple rectangular shape of figure 9(b).

Two-Microphone Intensity Measurement Technique

The measurement of intensity at an axial location in a duct can be viewed as an extension of the two-microphone technique used to determine acoustic impedances. The analytical basis for the measurement procedure has been developed by several investigators (e.g., see refs. 16, 17, and 18). In essence, the method involves a transfer function measurement between two points in the standing wave field generated by the incident and reflected waves on the test specimen. The analysis will be outlined here for completeness.

For plane waves, the acoustic pressures at locations x_1 and x_2 (see fig. 10) are defined as

$$p(x_1) = A(e^{ikx_1} + Re^{-ikx_1}) \quad (22)$$

and

$$p(x_2) = A(e^{ikx_2} + Re^{-ikx_2}) \quad (23)$$

Therefore, the transfer function between these two locations becomes

$$P_{12} = \frac{p(x_1)}{p(x_2)} = \frac{e^{ikx_1} + Re^{-ikx_1}}{e^{ikx_2} + Re^{-ikx_2}} \quad (24)$$

Equation (24) can be solved for the reflection factor R as

$$R = \frac{e^{ikx_1} - P_{12}e^{ikx_2}}{P_{12}e^{-ikx_2} - e^{-ikx_1}} \quad (25)$$

The acoustic intensity I can then be determined by

$$I(x_1) = \frac{1}{2} \text{Re}\{p(x_1)v^*(x_1)\} \quad (26)$$

where $v^*(x_1)$ is the complex conjugate of the acoustic velocity at location x_1 , as defined by

$$v(x_1) = \frac{A}{\rho c} [e^{ikx_1} - Re^{-ikx_1}] \quad (27)$$

Finally, the impedance ζ at the reference plane (looking from left to right in fig. 10) is determined by the

simple relation

$$\zeta = \frac{1 + R}{1 - R} \quad (28)$$

The accuracy of this method depends on the ability of the transfer function to provide sufficient information to reconstruct the standing wave pattern in the tube. The reconstructed wave pattern accuracy depends jointly on the accuracy of the transfer function measurement (amplitude ratio and phase difference) and on a judicious selection of the two microphone locations relative to the test specimen surface. Essentially, the method must be capable of reconstructing the "true" standing wave pattern in the sense that it should be indistinguishable from that obtained from a continuous traversing probe (see refs. 19 and 20). Clearly, the method relies on very accurate amplitude and phase calibration of the microphones, which is a tedious and, therefore, time-consuming procedure. This constitutes a major disadvantage of the method as reported in references 16, 17, and 18. With this difficulty in mind, the two-microphone data were acquired by traversing a single-probe microphone from one position to the other, thereby avoiding the need for tedious calibration procedures.

Results and Discussion

Impedance Measurements

Measurements of normal incidence impedance were obtained for both the round resonator arrays and the square resonator arrays. Figures 11 and 12 show the resistance and reactance, respectively, versus frequency for a cavity depth of 5.4 in. The data shown were taken for resonator 5 in the round and square arrays and for an incident sound pressure level of 120 dB. Data for the round and square resonators are depicted by the round and square symbols, respectively, and have been normalized by ρc . Figure 12(b) shows segments of the reactance data on an expanded scale in the vicinity of the first two resonances (i.e., zero reactance crossings).

The measured resistances for each of the two resonators are nearly constant with frequency, except in the neighborhood of the cavity antiresonances of 1.26 and 2.52 kHz (see fig. 11). The large increase in resistance near cavity antiresonant frequencies is characteristic of thin resistive face sheets backed by nondissipative cavities. For much smaller diameter cavities (i.e., narrow parallel channels) with no resistive face sheet, acoustic energy dissipation occurs mainly in the channel boundary layers. In this case, a transmission model (see ref. 21) that accounts for distributed dissipation predicts a gradual increase of the

channel entrance resistance as the channel antiresonant frequency is approached. In the limit of concentrating all the dissipation in a thin face sheet, a dramatic increase in the effective resistance near the resonator antiresonance is observed, which is consistent with the transmission line model. Because the backing cavities employed in the usual aircraft-type resonant duct liners have relatively large diameters (and, thus, negligible dissipation), a simplified model has been employed that adds the impedance of the face sheet to the reactance of the backing cavities. This model was also employed in the present investigation. Therefore, the resistance used in the propagation models was approximated by continuous, straight lines, faired through the data as shown. The measured resistance of the round resonator (which together with the face sheet forms a resonator element) is about 40 to 50 percent greater than that for the square resonator.

Reactance data over the frequency range 0.5 to 3.0 kHz are plotted in figure 12(a). As expected, the data follow a $-\cot(kL)$ trend as indicated by the dashed curves in the figure. In the vicinity of the antiresonance frequencies, 1.26 and 2.52 kHz, $-\cot(kL)$ becomes infinite. Resonance frequencies are defined by the zero reactance crossings at approximately 0.61, 1.82, and 3.12 kHz. To better observe the small perturbing effect of the fiber metal face sheet on the total reactance, the scale of the graph is expanded near the resonance frequencies as shown in figure 12(b). The fiber metal face sheet contributes a small positive reactance ($e^{i\omega t}$ time convention), as is evident in the figure. By comparing the first and third resonant frequencies with the corresponding $-\cot(kL)$ zero crossings, it is evident that this effect shifts the resonant frequencies to lower values and that the amount of shift increases with frequency. These observations are consistent with the small positive reactance associated with any thin, porous face sheet.

In view of the 45-percent difference between the acoustic resistances of resonator 5 of the round and square arrays, dc flow resistance measurements were conducted for all seven resonators of the two arrays to determine the resistive component variability. As described in the "Experimental Setup and Measurement Procedures" section, these measurements were accomplished by attaching a source of controlled air-flow to the resonator cavity and measuring the resulting volume flow and pressure drop across the fiber metal face sheet. Flow resistance data for all seven resonator elements of the round and square arrays are shown in figure 13. Note that the smallest incident velocity was about 70 cm/sec, which corresponds to a 140-dB incident plane wave. Since the

main purpose of these measurements was to evaluate resonator resistance variability, all measured flow resistances were extrapolated to zero velocity.

The zero velocity flow resistances, normalized by ρc , were plotted versus resonator location for both arrays and are presented in figure 14. The dashed lines represent average flow resistances of the two resonator arrays and serve as references for comparing the flow resistance variability of the two arrays. Note that the average flow resistance for the round resonator array is nearly twice that for the square resonator array. Also, the variability for the square resonator array was much less than that for the round resonator array. Visual inspection indicated differences in the fiber distribution densities and in the wicking of the bonding agent into the active area of the fiber metal. Thus, even though the two face sheets were taken from the same parent material with the intention of having equal resistances for the two arrays, significant differences in flow resistances were obtained that were apparently due to material inhomogeneities and bonding technique.

Broadband Acoustic Attenuation Measurements

The first series of acoustic attenuation measurements were performed using broadband noise to determine the effect of array orientation on the total attenuation across the array. Because of measurable differences in the resonator resistances, which resulted in an asymmetrical resistance distribution with respect to the midspan, or number 4, resonator (see fig. 14), attenuation measurements across the resonator arrays were conducted for both the forward and reverse orientations with respect to the sound propagation direction. The results are shown in figure 15 for the round and square resonator arrays at uniform cavity depths. Total attenuation was obtained by measuring the sound pressure at position B relative to that at position A, as indicated by the sketch in the figure. Sound propagates from left to right and encounters resonator 1 first in the forward orientation and resonator 7 first in the reverse orientation. Position A is located in the leading edge plane of the array and position B is located in the trailing edge plane. The attenuation data for each resonator orientation were plotted versus frequency between 0.3 kHz and 3.0 kHz as shown. The overall sound pressure level at the leading edge in all cases was 132 dB.

Figure 15(a) shows the comparison for the round resonator array. For this array, there is a small, but measurable, change in the attenuation between the two orientations, whereas for the square resonator array (fig. 15(b)) the change is barely detectable. These

observations are consistent with the greater variability and asymmetry about the midspan resonator in the round resonator resistances. A symmetrical variability of resonator resistances about the midspan resonator would not be expected to produce a change in attenuation upon orientation reversal.

Measured and Calculated Axial Attenuation Profiles

Figure 16 shows (for a representative set of frequencies) measured and calculated axial attenuation profiles over the length of the resonator arrays. These data were obtained with discrete frequency sound that was incident on the resonator array in the forward orientation. The cavity depths were set at their maximum of 5.4 in. Sound pressure levels for nine test frequencies in the neighborhood of the first resonance (610 Hz) were measured at axial distance intervals of 1 in., starting at the array leading edge. As indicated in the figure key, the shaded and open symbols represent the calculated and measured profiles, respectively. The calculation results presented here were performed with the finite element code, so that the complete attenuation profiles, including end effects, of the resonator array could be compared with the measured profiles. This necessitated that the equivalent length impedance distribution modeling procedure, depicted in figure 8(d), be employed for the round resonator array. Attenuation rates were extracted from the straight-line slopes of the linear regions of the profiles as indicated in figure 16.

For the round resonator array results shown in figure 16(a), the agreement between measured and calculated attenuation profiles is good to excellent, with at most a 1-dB underprediction for the 624-Hz test frequency. The agreement between measured and calculated attenuation rates, as determined from the linear portion of the profiles (see faired lines through data), is excellent. Thus, at least for no flow and for impedance nonuniformity separation distances up to 0.14 acoustic wavelengths, attenuation profiles are apparently well predicted by a finite element model that allows only axial impedance variations. For the square resonator array data presented in figure 16(b), the calculated and measured attenuation rates are still in good agreement, but there are significant differences between the measured and calculated profiles. At 500 Hz there is a 4-dB difference along the greater part of the array length. These differences seem surprising in that the measured resistances for the square resonator array exhibited much less variability than did those for the round resonator array, and the interstitial blockage is much less than that for the round resonator array. One possible explanation for the greater discrepancy

is that the square resonator resistances were much closer to the optimum value for this duct geometry than were the round resonator resistances. It is well known that attenuation rates become more sensitive to changes in impedance components in the neighborhood of the optimum impedance values (see ref. 22). For this duct geometry, the optimum nondimensional impedance at 600 Hz is about $0.16 - 0.14i$. At this frequency, the average nondimensional impedance is about $0.88 + 0.0i$ for the round resonator array and $0.45 + 0.0i$ for the square resonator array.

In figure 17, the axial attenuation rates for the two resonator arrays are expressed as decibels per duct height versus frequency or, alternatively, versus the nondimensional parameter kh , where k is the wave number and h is the duct height. Thus, these results can be applied to any geometrically similar duct with the same "equivalent" impedance distribution, provided incident energy is carried predominantly by the plane wave mode. The measured and calculated attenuation rates for the round and square resonators are shown by the round and square symbols, respectively. The attenuation rates in this case were calculated using the infinite waveguide, modal analysis, with both the smeared and equivalent length surface impedance distribution modeling procedures (see figs. 8(b) and (c)). The darkened symbols represent the smeared impedance distribution modeling procedure and the enclosed X symbols represent the equivalent length impedance distribution model (see fig. 8). The open symbols represent the measured attenuation rates as taken from the linear regions of the measured attenuation profiles of the type presented in figure 16.

A cursory examination of the data trends reveals that the maximum measured and calculated attenuation rates for the square resonator array are about twice those for the round resonator array. This observation again confirms that the average resistance of the square resonator array was nearer the optimum resistance for this particular duct geometry than was the round resonator array. Also, the calculated peak attenuations (darkened and enclosed X symbols) appear shifted to a somewhat higher frequency relative to the measured peak attenuations. This frequency shift of about 50 Hz is most likely due to the reactive impedance component being modeled as $-\cot(kL)$ without including the positive contribution from the face sheet. However, the calculated peak attenuations are within 1 dB of the measured values. Also, the two different surface impedance distribution modeling procedures result in at most a 1-dB difference in attenuation rates, with the equivalent length procedure being more conservative.

Figure 17(b) shows a similar comparison between measured and calculated attenuation rates from the finite element analysis method, which accounts for impedance variations in the axial direction and, therefore, finite length effects. In this calculation, the smeared impedance was used to model each individual resonator impedance as an equivalent rectangular region of impedance, as depicted in figure 8(b). As for the equivalent length impedance distribution model, this analytical method gives excellent agreement between measured and calculated results.

Since the duct height h and the separation distance between impedance nonuniformities are nearly equal (see fig. 1), the nondimensional frequency parameter kh also serves as a nondimensional measure of the impedance nonuniformity separation distance. The results of figures 16 and 17 suggest that the smeared and equivalent length impedance distribution modeling procedures are equally reliable for values of kh up to at least 0.8. Even though the predicted attenuation profiles apparently become less accurate as the modeled impedance approaches an optimum value, predicted and measured attenuation rates are still in reasonably good agreement. This circumstance may be due to the increasingly critical role of end reflections as the impedance approaches optimum. A complicating factor in this argument is the greater variability of the round resonator resistances as compared with those of the square resonator array. However, it is believed that this variability can be discounted because very little change in the total attenuation spectrum occurs when the array orientation is reversed, as shown in figure 15.

Measured and Calculated Transmission Losses

Next, comparisons of measured and calculated transmission losses for three different cavity depth configurations of the round resonator array were performed. No further tests were performed on the square resonator array because of inadvertent physical damage. Measured transmission losses were obtained from incident and transmitted net intensities as described in the "Experimental Setup and Measurement Procedures" and "Analysis" sections. The baseline test configuration consisted of all cavity depths set at a uniform depth of 5.4 in. The second configuration consisted of a linear variation of the cavity depths varying from 5.4 in. at the leading edge to 1.3-in. at the trailing edge. The third configuration consisted of the same linear variation and orientation, but with the cavity depths reversed so that the sound encountered the 1.3-in. cavity first. These configurations are depicted in sketches, along with the corresponding test results, in figure 18.

Figure 18(a) shows the measured and calculated transmission losses for the uniform cavity depth configuration. The open and darkened symbols represent the measured and calculated values, respectively, of the transmission losses. The measurements were obtained at 50-Hz intervals from 0.3 to 3.0 kHz. Calculations were done at 12 frequencies that included the first two resonances. The trends for the calculated data follow very well those for the measured data. For the second resonance, in the neighborhood of 1.8 kHz, the calculated data points are shifted about 10 Hz toward higher frequencies relative to the measured trend. This difference is apparently due to small systematic errors in the reactive impedance component.

For the low frequency, broadband noise suppression application envisioned for resonator arrays of this type, it is desirable that the passbands associated with the antiresonant frequencies be eliminated as much as possible. The staggered tuning, or variable cavity depth, configurations to be discussed next are an attempt to accomplish this result.

Figure 18(b) shows measured and calculated transmission losses for a linearly varying cavity depth configuration, as depicted by the sketch in the figure. Note that less transmission loss variation with frequency is observed in comparison with the uniform depth configuration. Specifically, the transmission loss extrema over the frequency range of interest are observed to decrease from 1 and 22 dB for the uniform cavity depth configuration to approximately 5 and 15 dB for the two variable cavity depth configurations. Thus, the trade-off for increasing the transmission losses at the minima is apparently a substantial reduction at the transmission loss maxima, at least for this configuration.

The calculated transmission loss trend tracks that of the measured values, with at most a difference of 1 dB in the vicinity of the resonant peaks. It is not clear why there is more discrepancy between measured and calculated results for the variable cavity depth configuration than for the uniform depth configuration. One possibility is that the axial variation in the resonator resistances becomes more important when an axial variation in the resonator reactances is present.

To further investigate the effect of axial variation in the resonator array reactance, the linear variation in cavity depths was reversed with respect to the sound propagation direction (i.e., the first resonator encountered by the sound was set at the minimum depth of 1.3 in.). Measured and calculated transmission losses for this configuration are presented in figure 18(c). Again, the general trend of the measured transmission losses is well predicted by the

theoretical model. However, the calculated transmission losses range both above and below the measured results by about 1.5 dB. Thus, there is no significant difference in the ability of the theoretical model to predict the results for the two configurations depicted in figures 18(b) and 18(c). The chief difference in the overall transmission loss behavior for the two variable depth configurations would likely be the substantially different reflection experienced by the incident wave upon encountering the initial resonator.

Effects of Mean Flow on Resonator Array Attenuation

The final results to be discussed in this investigation concern the effect of mean flow on the round resonator array attenuation. Tests were done at mean flow Mach numbers of 0.1 and 0.3 and for the uniform cavity depth configuration. Corresponding flow profiles are shown in figure 19. Changes in total attenuation across the array relative to that for the no-flow condition are plotted in figure 20 versus the excitation frequency or, alternatively, the nondimensional frequency parameter kh . Data were obtained at 10 discrete test frequencies at approximately equal intervals from 0.3 to 3.0 kHz that included both resonant and antiresonant frequencies. Attenuation changes are referenced to the no-flow attenuation as measured with broadband noise (see fig. 15(a)). Note that the changes in attenuation are presented in terms of the total attenuation across the resonator array, as opposed to the attenuation per duct height.

Clearly, there is a substantial effect of the mean flow at the resonant frequencies for the higher flow Mach number of 0.3. For the flow Mach number of 0.1, the effect is not very significant. It is unlikely that these attenuation changes are due to flow-induced changes in the resonator impedance since, according to reference 23, fiber metal face sheets exhibit little resistance change for modest mean flows of the magnitude examined here. More likely, the attenuation change is due to convection effects.

Of the two propagation models examined in this investigation, the finite element model offers more flexibility in dealing with realistic geometries. Also, the measured and predicted results for the no-flow condition were in measurably better agreement than for the modal decomposition propagation model. Thus additional tests were conducted at the higher flow speed ($M = 0.3$) to further validate the finite element model in the presence of flow. Again, these tests were performed with the uniform cavity depth configuration. Since the data of figure 16 indicated a large sound pressure level (SPL) attenuation across the liner at 624 Hz, that frequency was chosen for these comparisons. Figure 21 presents

analytical predictions for $M = 0$ and $M = \pm 0.3$ in a color format that qualitatively depicts the SPL variations throughout the test section in the resonator array region. As indicated in the legend, the SPL increases in intensity as the color changes from the black end to the white end of the color spectrum. It should also be noted that, for convenience, the resonators are assumed to be on the upper wall in the color graphs. The resonator positions are indicated to scale by the shaded areas at the top of each color contour plot. An intriguing difference between the no-flow data and the flow data is the variability of SPL across the duct in the presence of flow, as compared with the constant SPL across the duct at particular axial locations with no flow. It is also interesting to note the small-scale ripples superimposed on the larger scale color gradations in the vicinity of the resonators. These predicted "hot spots" are apparently due to flow effects, as they are entirely absent with no flow. Figure 21 also presents quantitative data in the usual attenuation profile form as centerline SPL versus axial distance for each of the flow conditions. As would be expected on the basis of convection effects, attenuations are less for positive flow (i.e., flow with sound) or greater for negative flow (i.e., flow against sound), respectively, than for no flow.

To verify that the analytically predicted hot spots near the resonator array in the presence of flow were real, and not just an artifact of the finite element numerics, a series of measurements of axial attenuation and phase variation were made along a 20-in. length of the test section that included the array, and at five heights above the array. These results are compared with the analytical predictions at those particular heights in figure 22. Figure 22(a) shows the no-flow behavior to provide a baseline for comparisons. Figures 22(b)–(f) shows flow effects in five parts, for a flow Mach number of 0.3 and y ranging from 0.19 in. to 1.06 in. These data clearly demonstrate that the model is capable of predicting not only the smooth trends of the no-flow condition, but also the spatial variability measured in the presence of flow. As seen in figures 22(b)–(f), the analytical model predicts the experimental measurements in remarkable detail for both the SPL and the phase, at each of the heights investigated. It should be recalled that no changes in the impedance due to flow effects are assumed in the propagation model.

The results presented in this report indicate that the modal decomposition model predicts duct liner attenuation rates to within about 1 dB per duct height for the smeared impedance distribution modeling procedure for kh values up to at least 0.8. The kh value of 0.8 also approximates the largest

nondimensional length scale of the axial impedance nonuniformities intrinsic to the round resonator array for these particular tests. The resistive component of the round resonator impedance was well off the optimum value for plane waves propagating in the present duct geometry, whereas the resistive component for the square resonators was nearer the optimum. This circumstance, which was unplanned in this experiment, indicates that further work should be done in which the round resonator impedance is near optimum. Based on limited tests with the square resonator, spatial nonuniformities in the impedance may be far more critical for the round resonator array near optimum impedance values. Comparisons of the finite element model predictions with measurements suggest, however, that this propagation model should be capable of accurately predicting detailed variations in the acoustic field near the resonator array in the presence of flow and near optimum impedance values. However, it was not within the scope of this investigation to perform tests at this condition.

Concluding Remarks

The objective of this investigation was to evaluate two particular analytical models, together with two different impedance distribution modeling procedures, for predicting the performance at low frequencies of duct liner configurations built with individually tuned resonators. These analytical models had previously been developed to predict the high frequency attenuation of aero-engine inlet duct liners, but no satisfactory validation of their accuracy existed in the low frequency range. In the low frequency application only the plane wave propagation mode exists, but the liner impedance is unavoidably characterized by a spatially varying impedance distribution whose length scale may be a significant fraction of the acoustic wavelength. This spatial impedance variation is a consequence of available structural components and fabrication techniques.

A "smeared" impedance modeling procedure was used to remove the transverse and axial impedance variations so that a modal decomposition propagation model could be used to predict attenuation rates. An equivalent length distribution procedure was used to remove the transverse impedance variation so that a two-dimensional (2-D) finite element propagation model could be used to predict attenuation profiles with the axial impedance variations left intact. Some of the more significant results of this investigation were as follows:

- Predicted and measured transmission losses for frequencies ranging beyond the second resonance of the resonator cavity were in very good agreement for all resonator cavity depths set the same
- For linearly varying cavity depths, predicted and measured transmission losses were still in good agreement, but less so than for the uniform cavity depths
- Generally, the transmission loss peaks and valleys were less prominent for the array configuration with linear cavity depth variation
- Significant changes in the transmission loss behavior were observed when the array orientation (with linearly varying cavity depths) was reversed with respect to the sound propagation direction

Finally, the most interesting and conclusive evidence for the validity of the finite element model was discovered when a set of detailed calculations of attenuation and phase profiles near the resonator array, with mean flow present, revealed a fine-scale structure of acoustic "hot spots" superimposed on the general acoustic field structure. Careful measurements verified the existence of such hot spots, which apparently are attributable to convective effects alone, since no flow-induced impedance changes were assumed in the model. The physics of this phenomenon is not clear. It is apparently associated with flow interaction with the acoustic field by means of the nonuniformities in the surface impedance distribution. Clearly, this is an item for further research.

The comparison of predicted and measured acoustic performances of the models discussed in this report shows that both the 2-D modal decomposition and 2-D finite element propagation models give good agreement with experiment. In addition, it has been demonstrated that the finite element model, in particular, is capable of predicting, to a remarkable degree, the detailed variation of sound pressure level in the presence of flow along a boundary of varying impedance. The work described in this report also shows that accurate experimental measurement of sound attenuation is a complex task requiring highly specialized equipment. Even in a relatively simple geometrical configuration, significant errors can be introduced when measurements do not include the detailed mapping of acoustic flux.

NASA Langley Research Center
Hampton, Virginia 23665-5225
November 17, 1987

References

1. Holmes, Bruce J.; Obara, Clifford J; and Yip, Long P.: *Natural Laminar Flow Experiments on Modern Airplane Surfaces*. NASA TP-2256, 1984.
2. Hefner, Jerry N.; and Bushnell, Dennis M.: *Status of Linear Boundary-Layer Stability Theory and the e^n Method, With Emphasis on Swept-Wing Applications*. NASA TP-1645, 1980.
3. Shapiro, Paul J.: *The Influence of Sound Upon Laminar Boundary Layer Instability*. Rep. No. 83458-83560-1 (Grant NSF Eng 75-17374 and Contract No. N00014-76-C-0396), Acoust. & Vib. Lab., Massachusetts Inst. Technol., Sept. 1977. (Available from DTIC as AD A046 057.)
4. Maestrello, Lucio: Active Transition Fixing and Control of the Boundary Layer in Air. AIAA-85-0564, Mar. 1985.
5. Abrahamson, A. Louis: *A Preliminary Design Study on an Acoustic Muffler for the Laminar Flow Transition Research Apparatus*. NASA CR-172374, 1984.
6. Lowson, M. V.: Duct Acoustics and Mufflers. *Aircraft Noise Generation, Emission and Reduction*, AGARD-LS-77, June 1975, pp. 7-1-7-34.
7. Hubbard, Harvey H.; and Manning, James C.: *Aeroacoustic Research Facilities at NASA Langley Research Center—Description and Operational Characteristics*. NASA TM-84585, 1983.
8. Parrott, Tony L.; and Jones, Michael G.: *Pressure Probe and Hot-Film Probe Responses to Acoustic Excitation in Mean Flow*. NASA TP-2581, 1986.
9. Watson, Willie R.: *A Finite Element Simulation of Sound Attenuation in a Finite Duct With a Peripherally Variable Liner*. NASA TM-74080, 1977.
10. Watson, Willie; and Lansing, Donald L.: *A Comparison of Matrix Methods for Calculating Eigenvalues in Acoustically Lined Ducts*. NASA TN D-8186, 1976.
11. Watson, Willie R.: *Noise Suppression Characteristics of Peripherally Segmented Duct Liners*. NASA TP-1904, 1981.
12. Abrahamson, A. Louis: *ADAM—An Axisymmetric Duct Aeroacoustic Modeling System*. NASA CR-3668, 1983.
13. Abrahamson, A. L.: *ADAM—An Axisymmetric Duct Aeroacoustic Modeling System*. AIAA-83-0666, Apr. 1983.
14. Dahlquist, Germund; and Björck, Åke (Ned Anderson, transl.): *Numerical Methods*. Prentice-Hall, Inc., c.1974.
15. Abrahamson, A. L.: *A Finite Element Algorithm for Sound Propagation in Axisymmetric Ducts Containing Compressible Mean Flow*. NASA CR-145209, 1977.
16. Seybert, A. F.; and Ross, D. F.: Experimental Determination of Acoustic Properties Using a Two-Microphone Random-Excitation Technique. *J. Acoust. Soc. America*, vol. 61, no. 5, May 1977, pp. 1362-1370.
17. Seybert, A. F.; and Parrott, T. L.: *Impedance Measurement Using a Two-Microphone, Random-Excitation Method*. NASA TM-78785, 1978.
18. Chung, J. Y.; and Blaser, D. A.: Transfer Function Method of Measuring Acoustic Intensity in a Duct System With Flow. *J. Acoust. Soc. America*, vol. 68, no. 6, Dec. 1980, pp. 1570-1577.
19. Impedance and Absorption of Acoustical Materials by the Tube Method. ASTM Designation: C384-58 (Reapproved 1972). Part 18 of 1975 *Annual Book of ASTM Standards*, c.1975, pp. 115-126.
20. Parrott, Tony L.; and Smith, C. D.: *Random and Systematic Measurement Errors in Acoustic Impedance as Determined by the Transmission Line Method*. NASA TN D-8520, 1977.
21. Parrott, Tony L.; Watson, Willie R.; and Jones, Michael G.: *Experimental Validation of a Two-Dimensional Shear-Flow Model for Determining Acoustic Impedance*. NASA TP-2679, 1987.
22. Lester, Harold C.; and Posey, Joe W.: *Optimal One-Section and Two-Section Circular Sound-Absorbing Duct Liners for Plane-Wave and Monopole Sources Without Flow*. NASA TN D-8348, 1976.
23. Hersh, A. S.; and Walker, B.: *Effects of Grazing Flow on the Steady-State Flow Resistance and Acoustic Impedance of Thin Porous-Faced Liners*. NASA CR-2951, 1978.

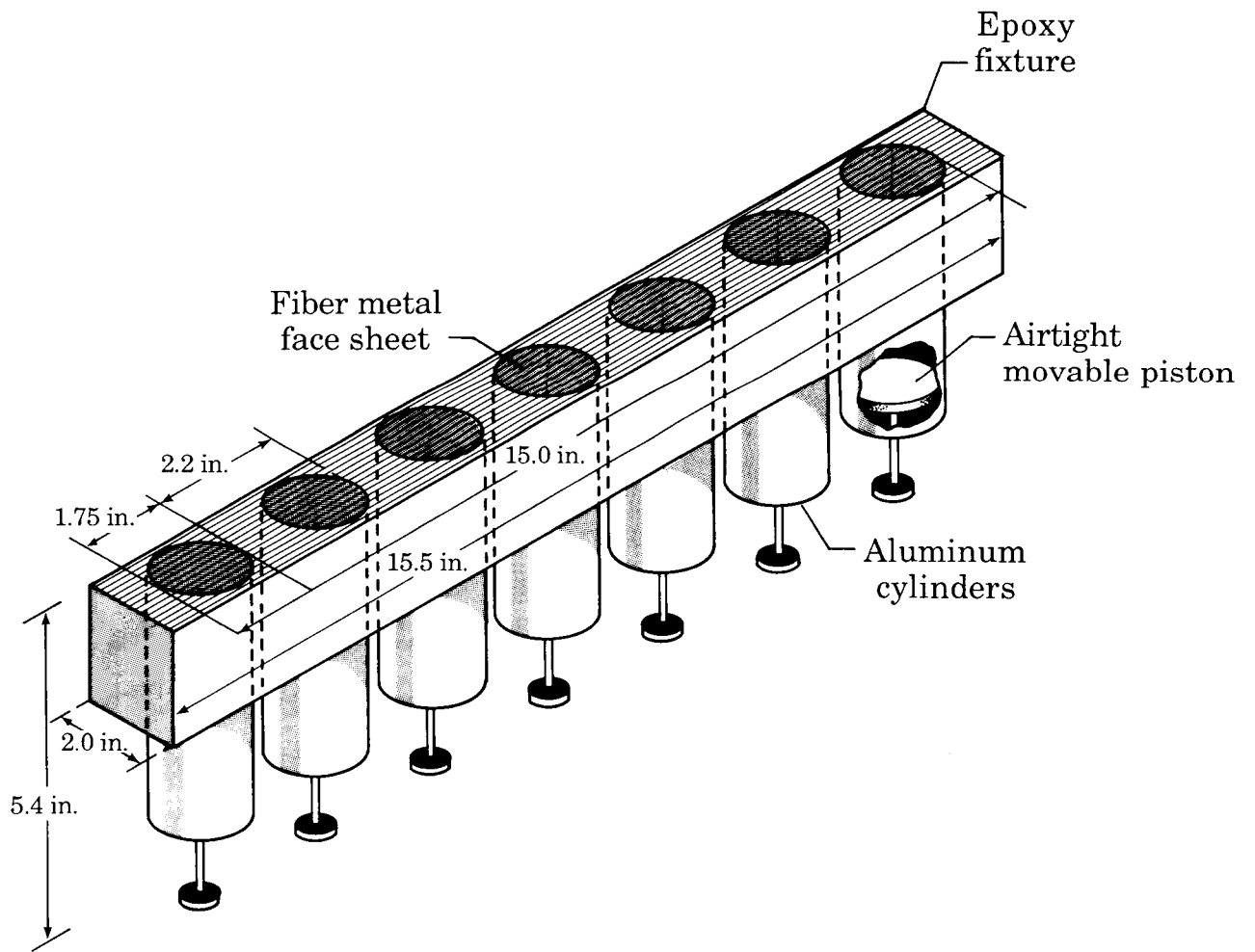


Figure 1. Sketch of round cavity resonator array.

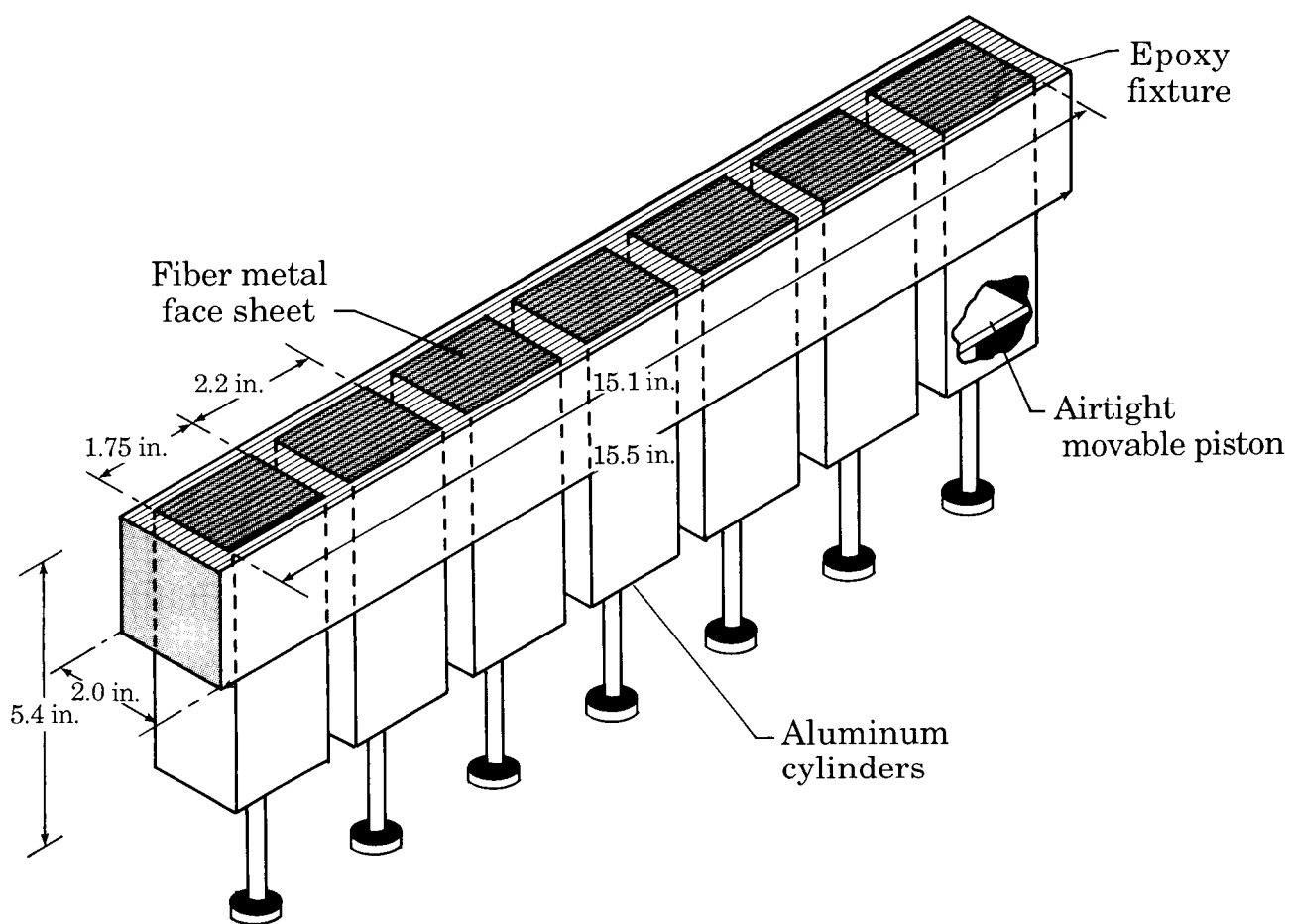
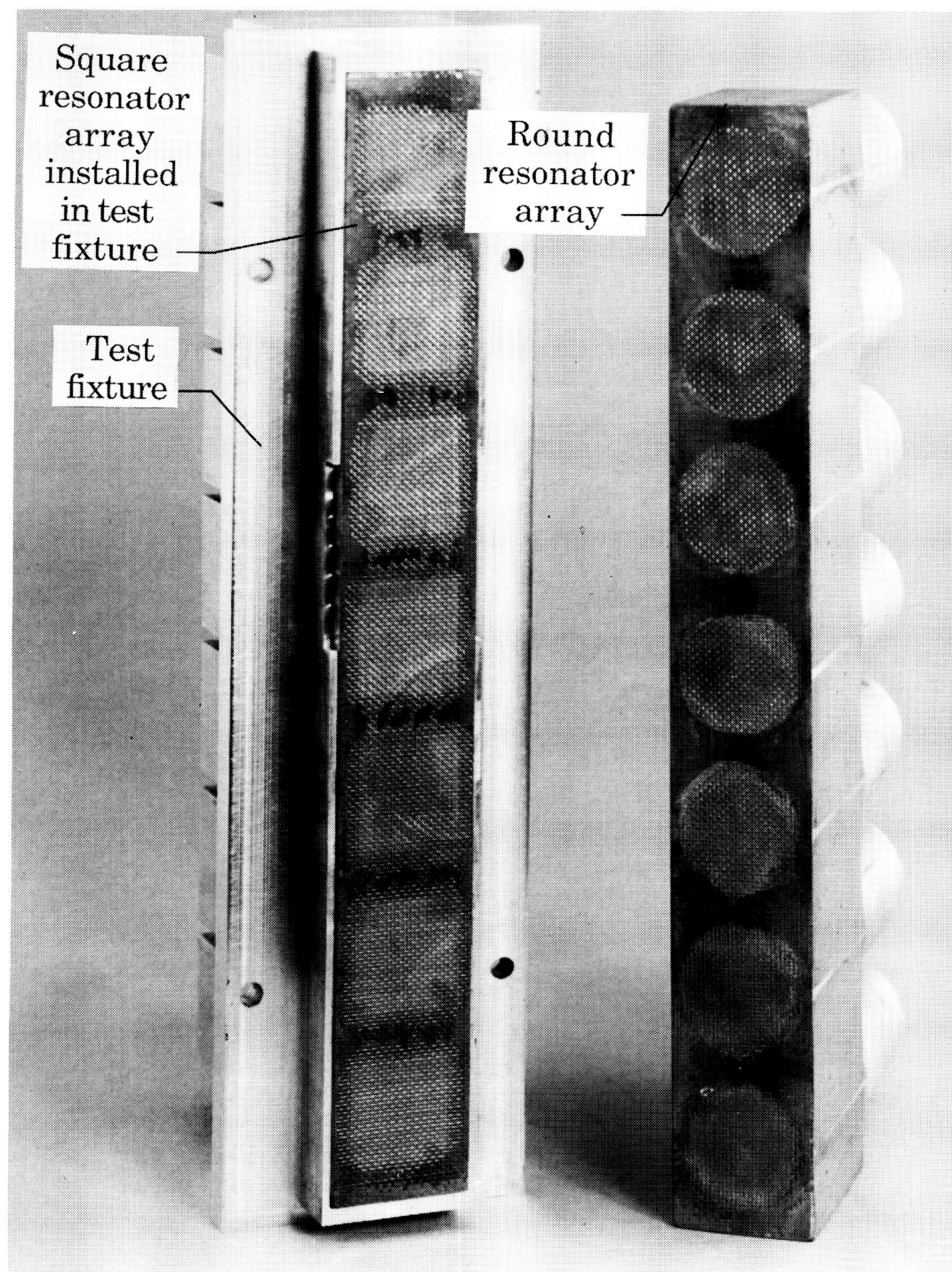


Figure 2. Sketch of square cavity resonator array.

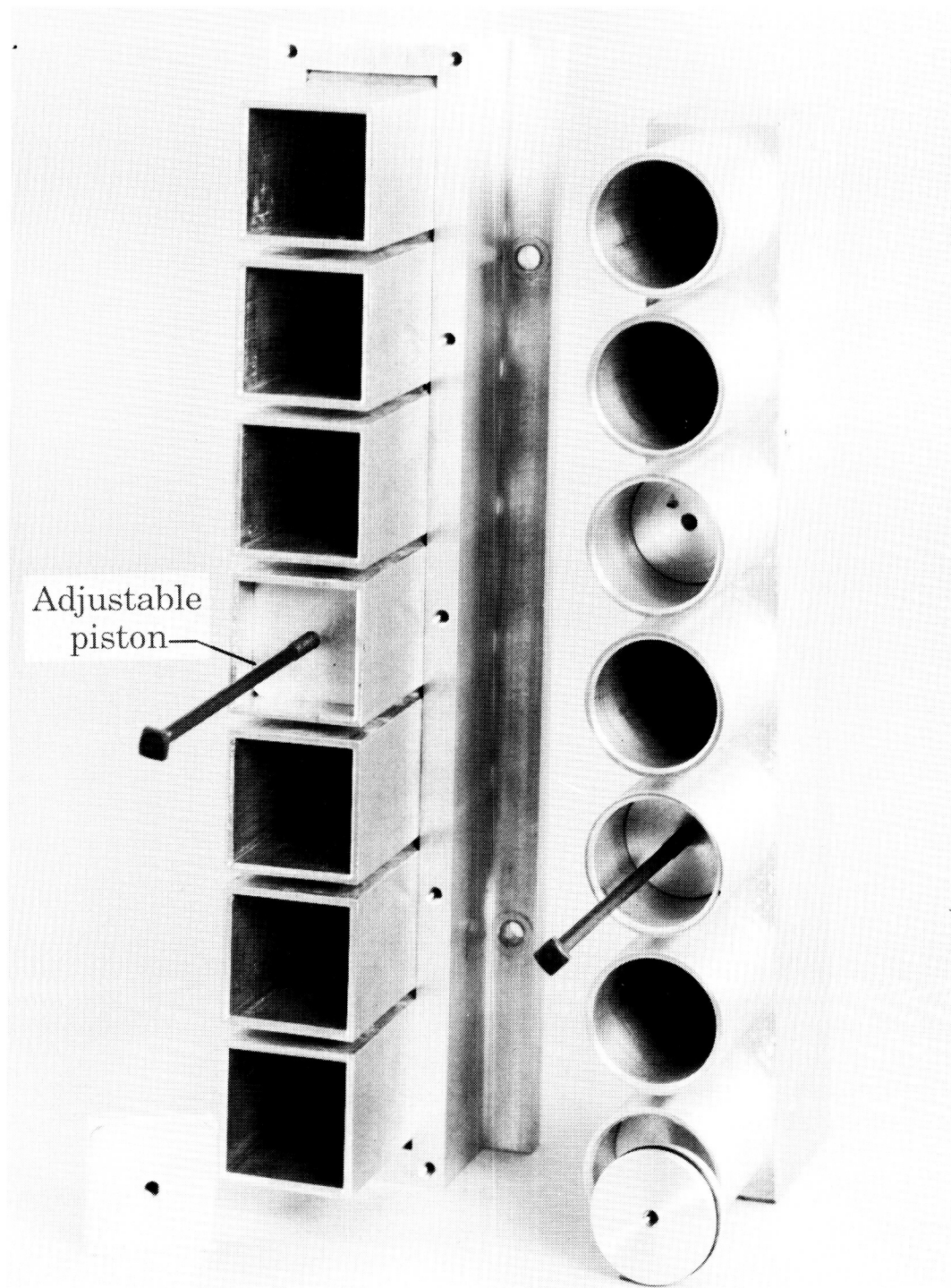
~~ORIGINAL~~ PAGE IS
~~OF POOR~~ QUALITY



L-86-255

(a) Front view.

Figure 3. Photograph of square and round resonator arrays showing fiber metal face sheet.



(b) Rear view.

Figure 3. Concluded.

L-86-260

ORIGINAL PAGE IS
OF POOR QUALITY

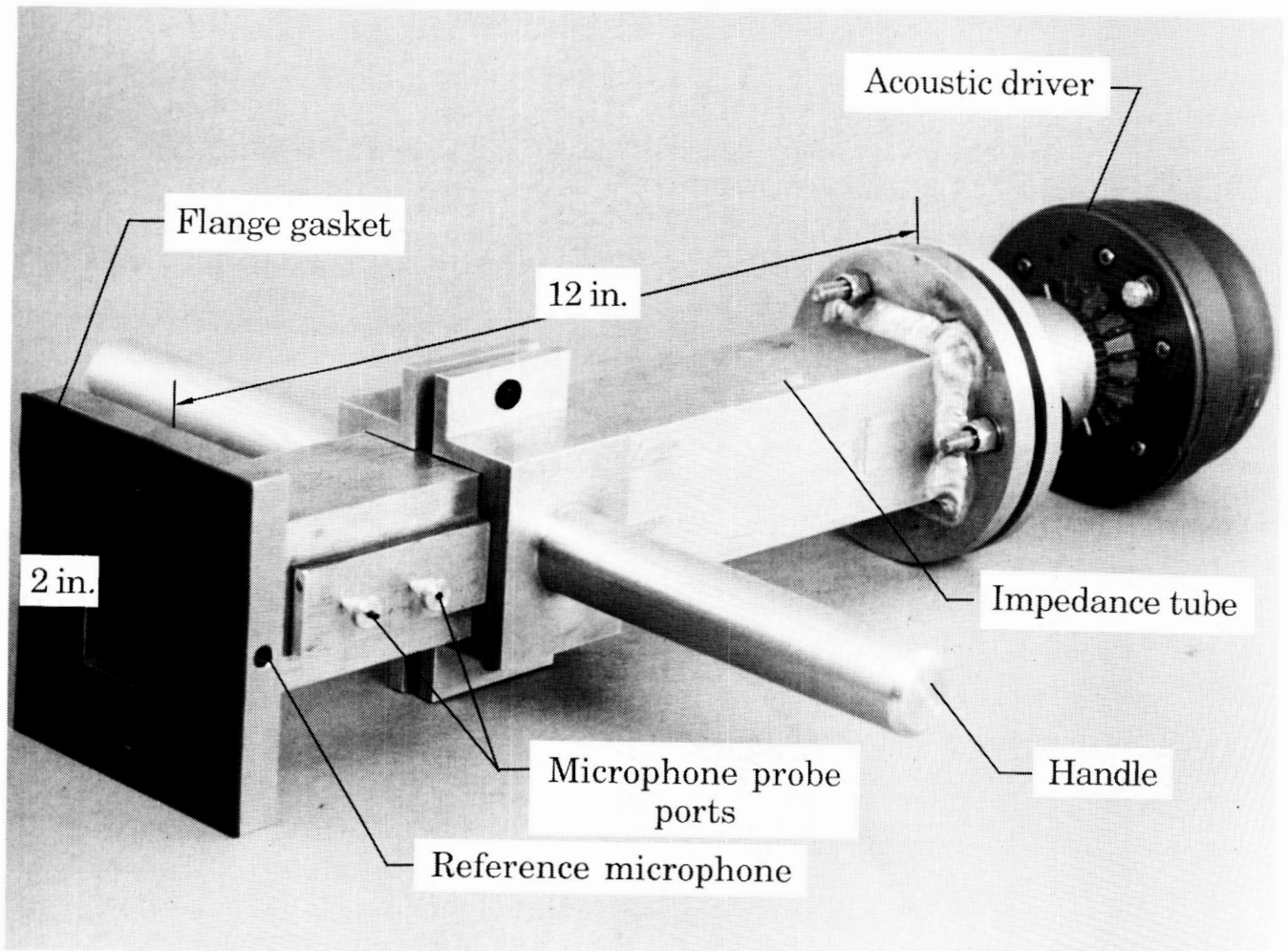


Figure 4. Normal incidence impedance tube for measuring impedances of square resonators.

L-86-258

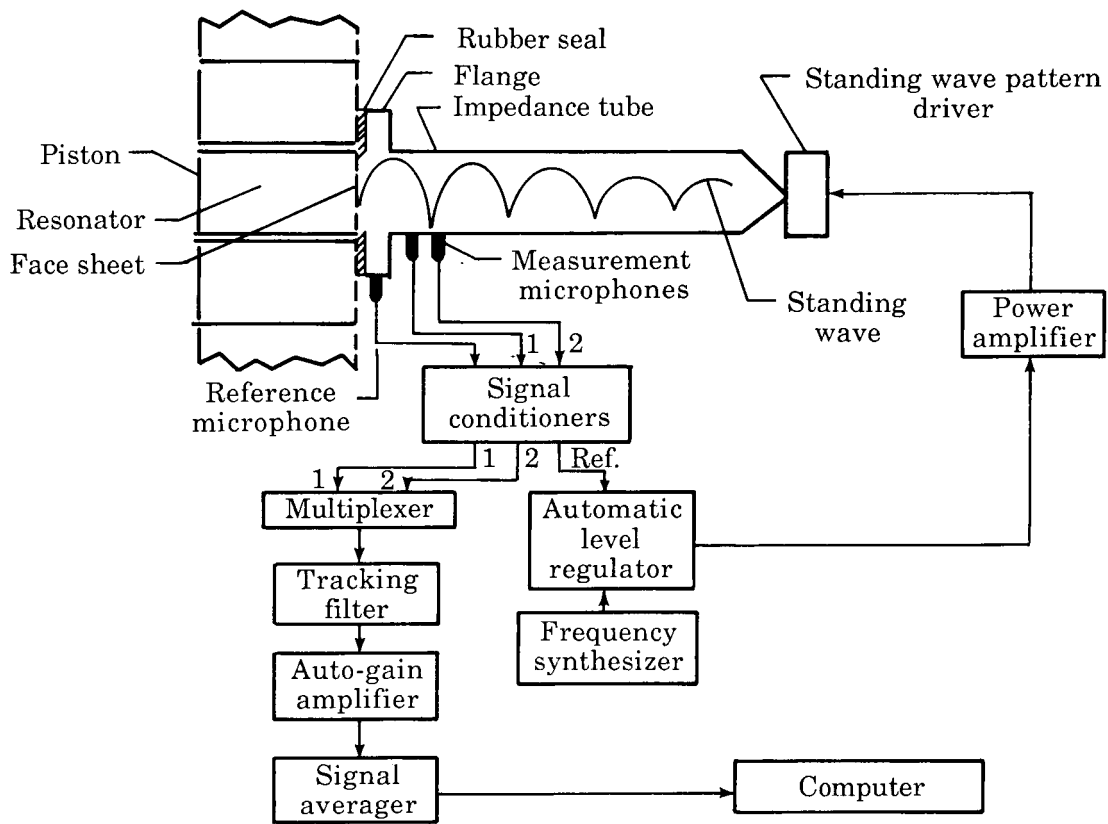


Figure 5. Schematic of normal incidence impedance measurement apparatus and instrumentation.

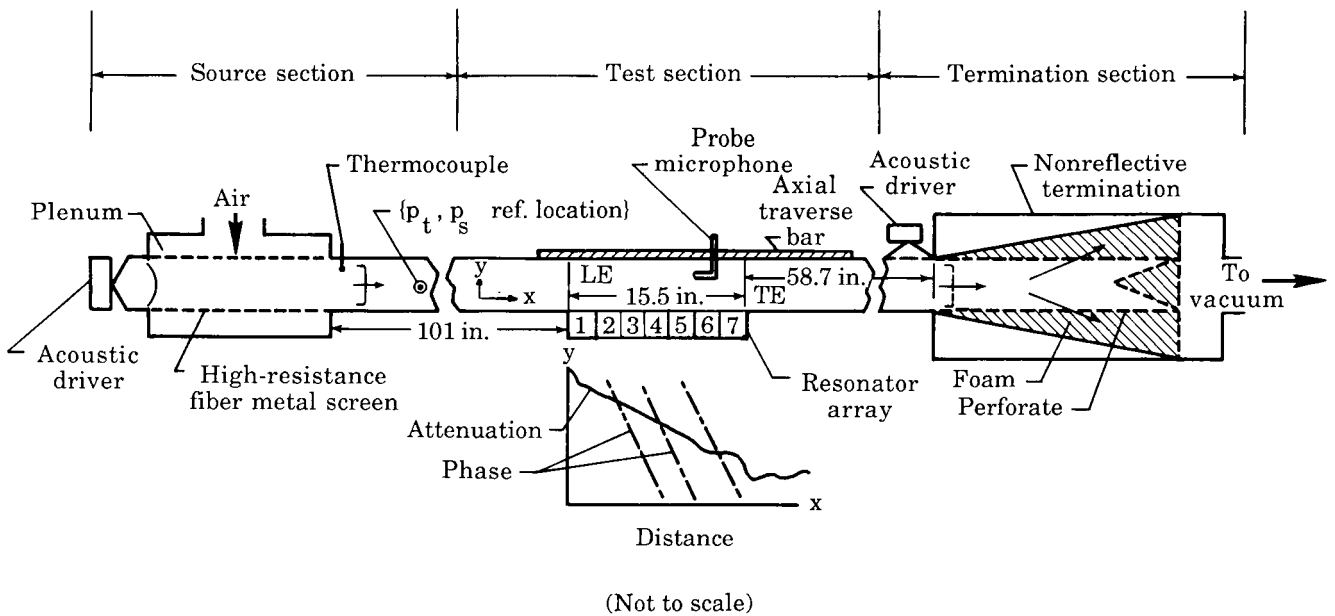
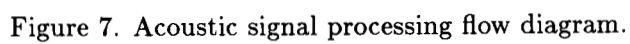
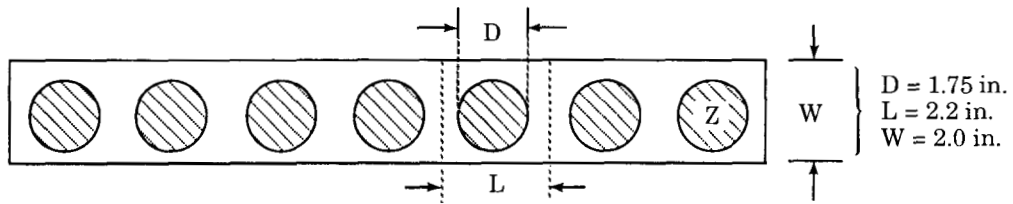
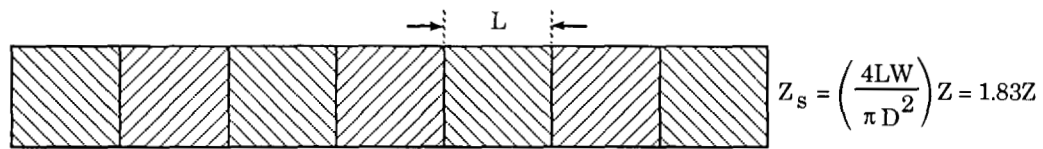


Figure 6. Schematic of experimental arrangement.

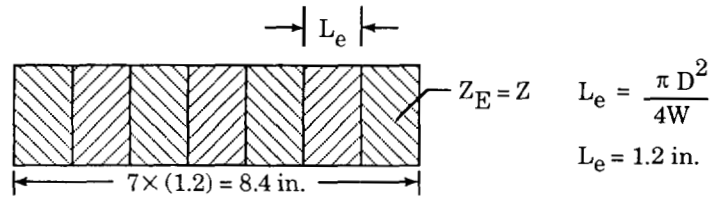




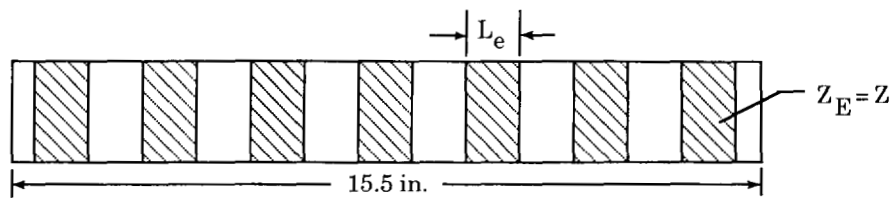
(a) Actual geometry.



(b) Smeared impedance model (modal decomposition program).

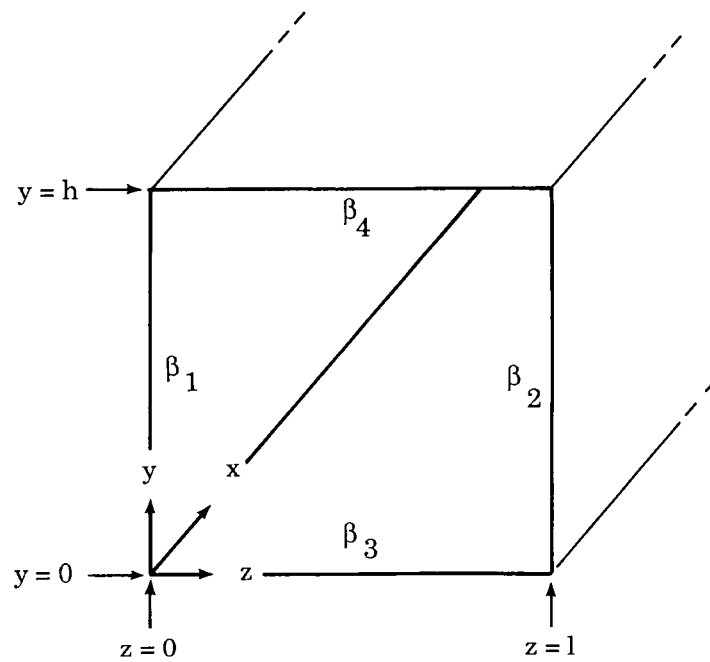


(c) Equivalent length model (modal decomposition program).

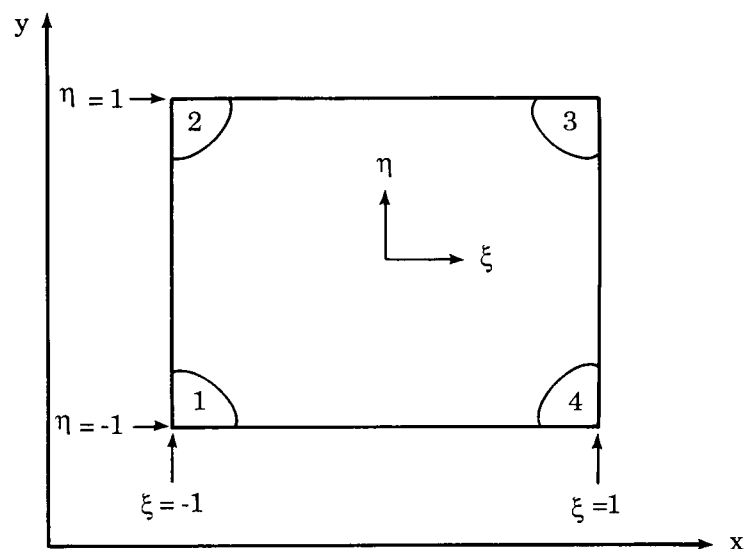


(d) Equivalent length model (finite element program).

Figure 8. Impedance models for round resonator array.



(a) Modal decomposition program.



(b) Rectangular four-node finite element program.

Figure 9. Coordinate systems used in analyses.

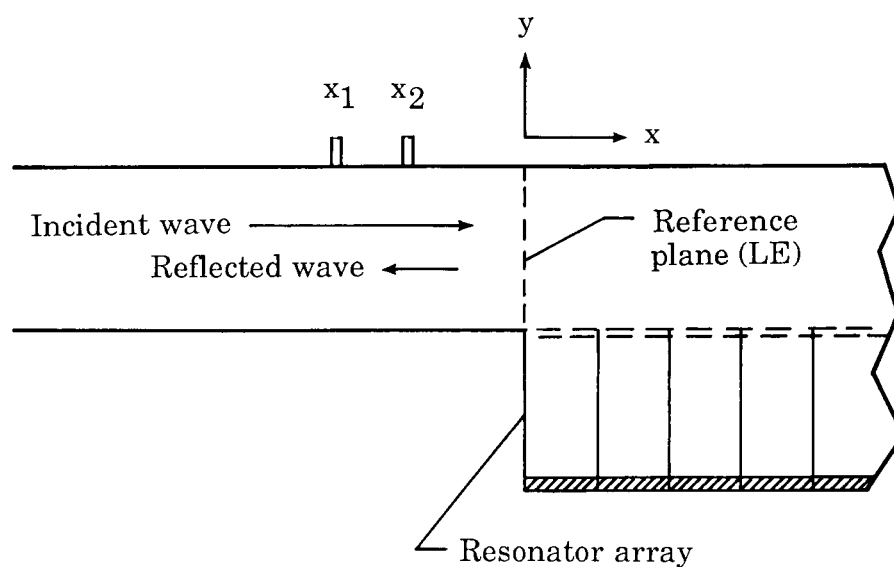


Figure 10. Coordinate system for two-microphone intensity measurement.

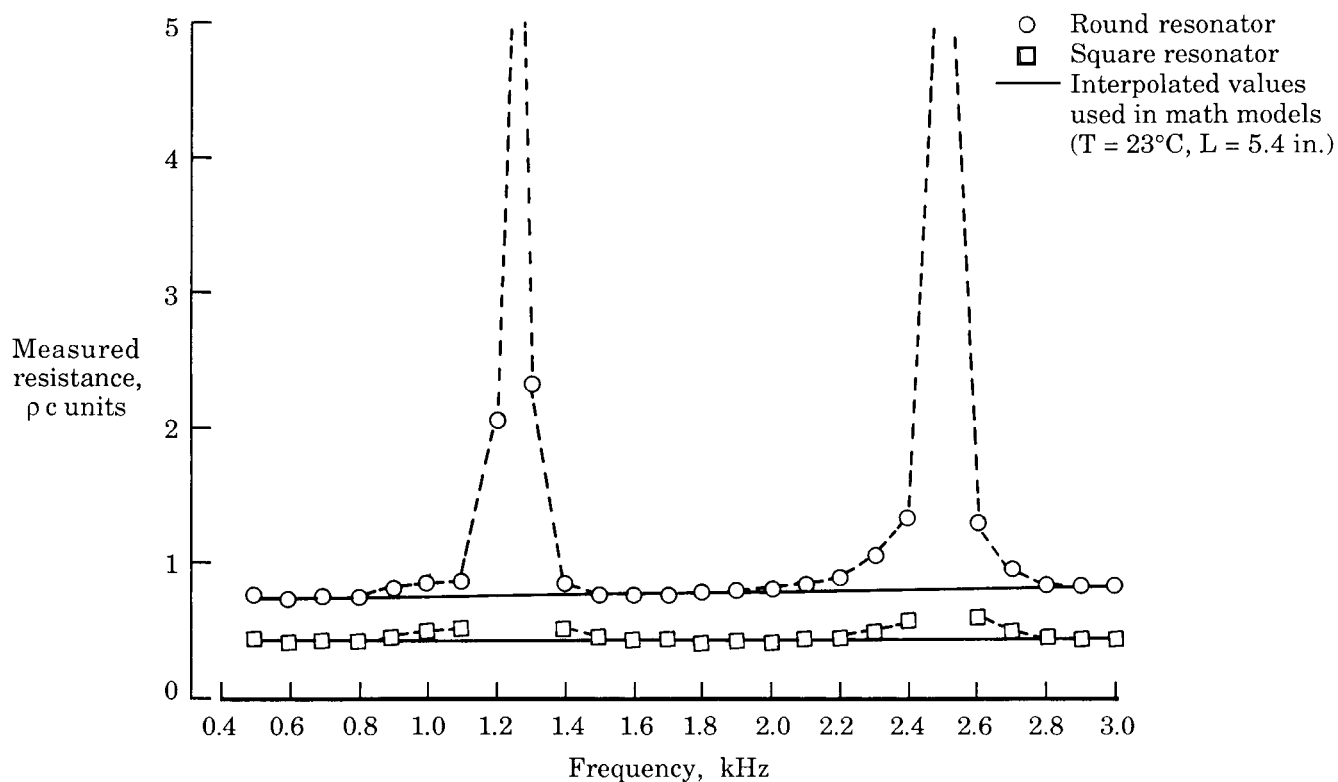
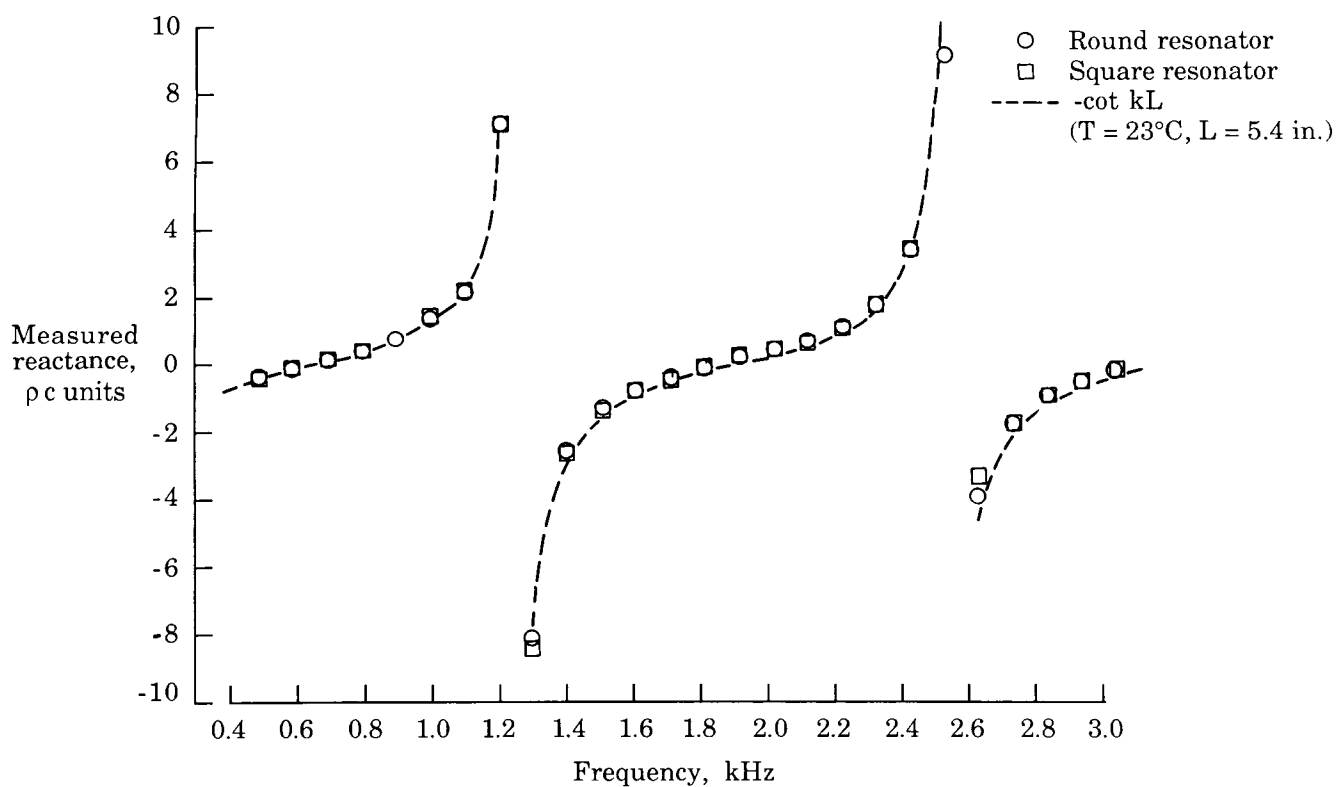
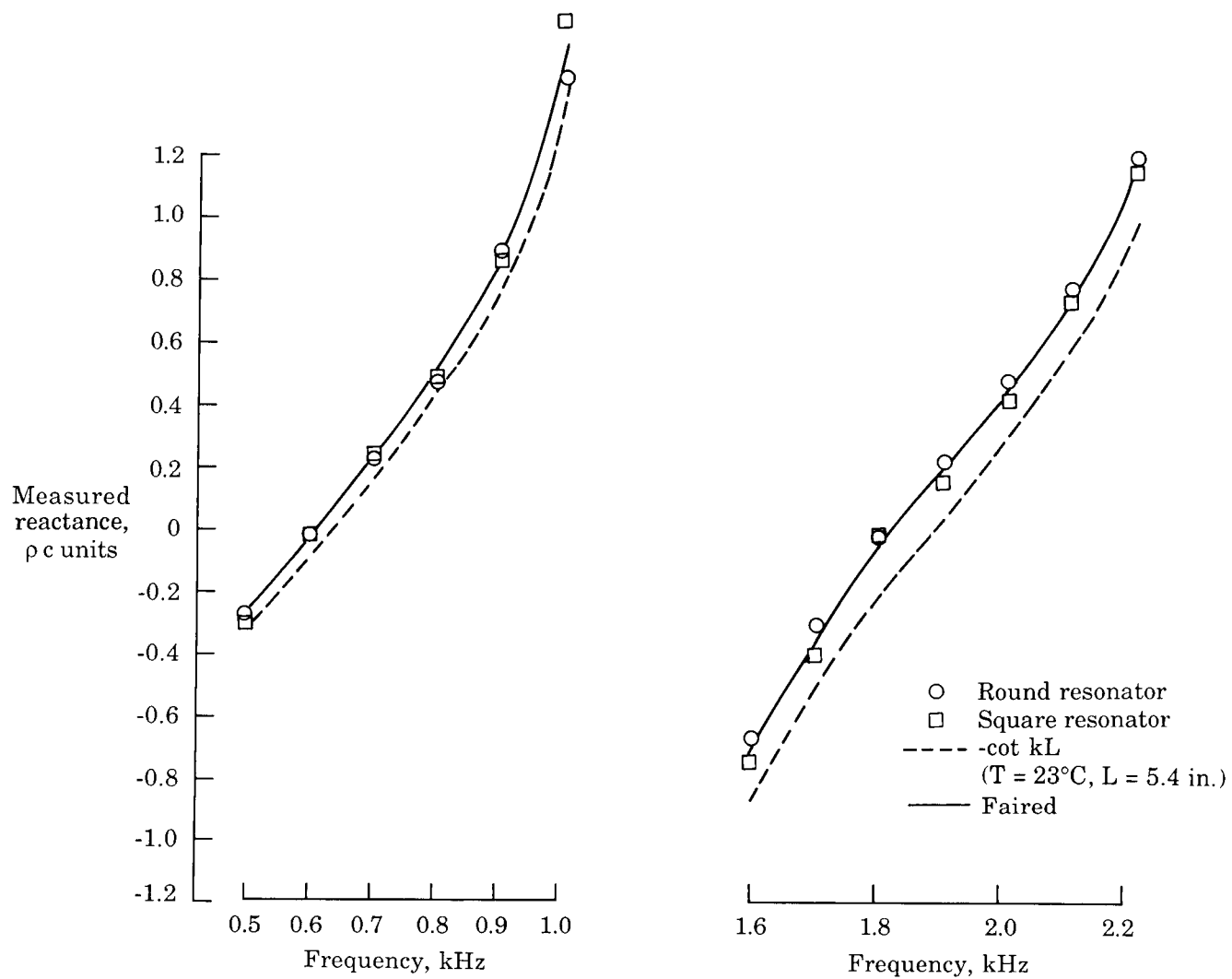


Figure 11. Measured resistance of round and square cavity resonators (resonator 5 in fig. 6).



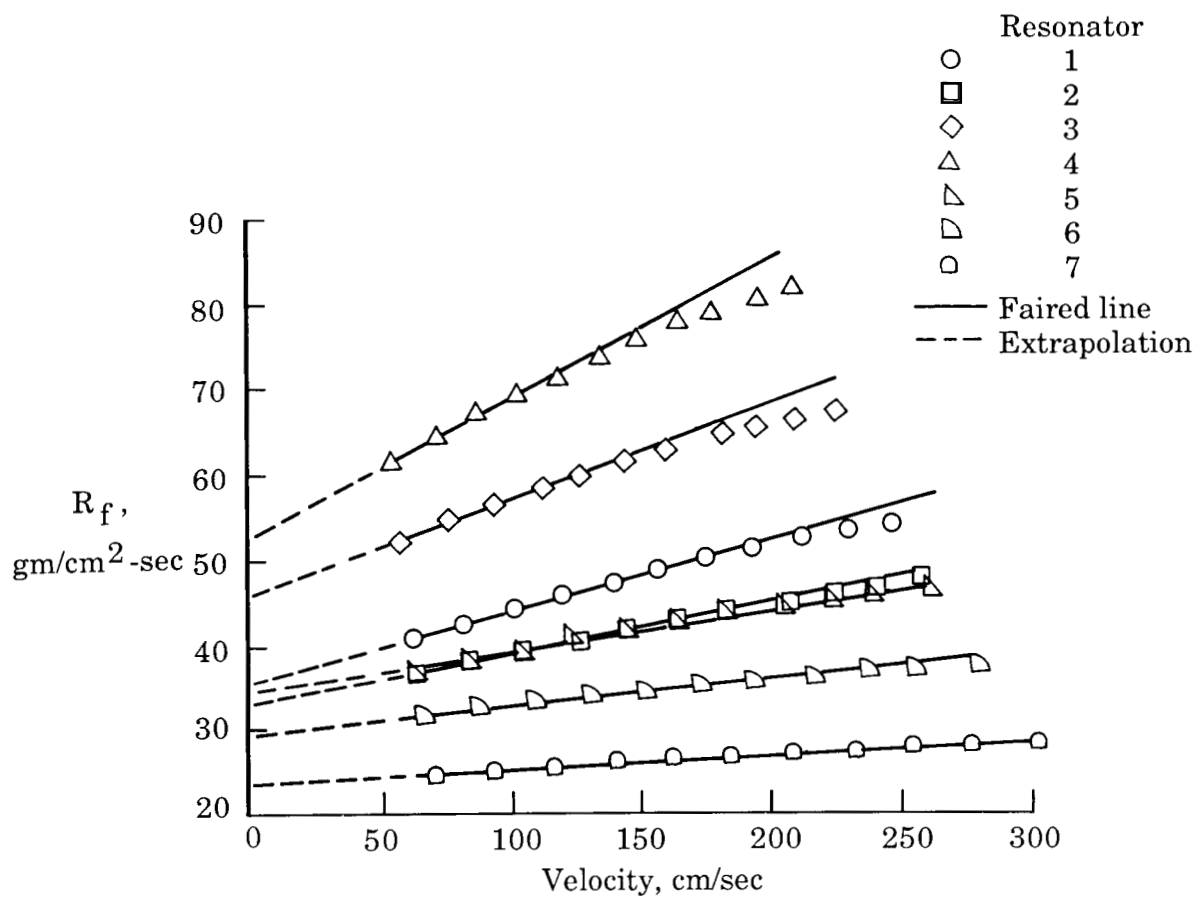
(a) Over frequency range 0.4 to 3.0 kHz.

Figure 12. Measured reactance of round and square cavity resonators.

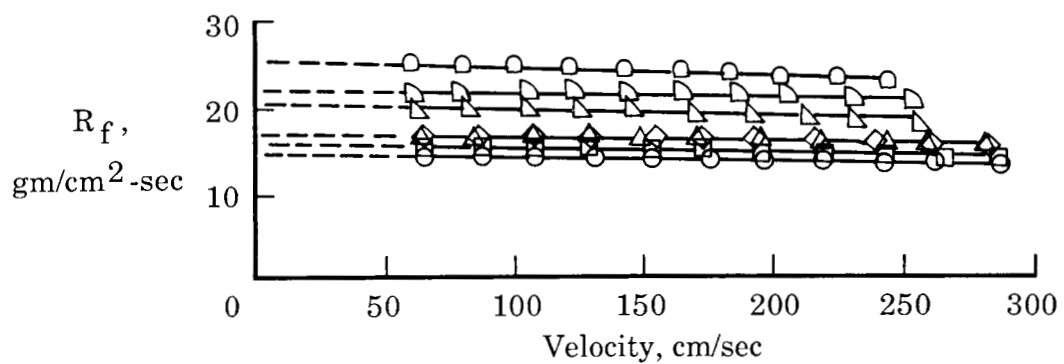


(b) Over frequency ranges in neighborhood of first two cavity resonances.

Figure 12. Concluded.



(a) Round resonator array.



(b) Square resonator array.

Figure 13. Flow resistance measurements for individual resonator array resistive elements.

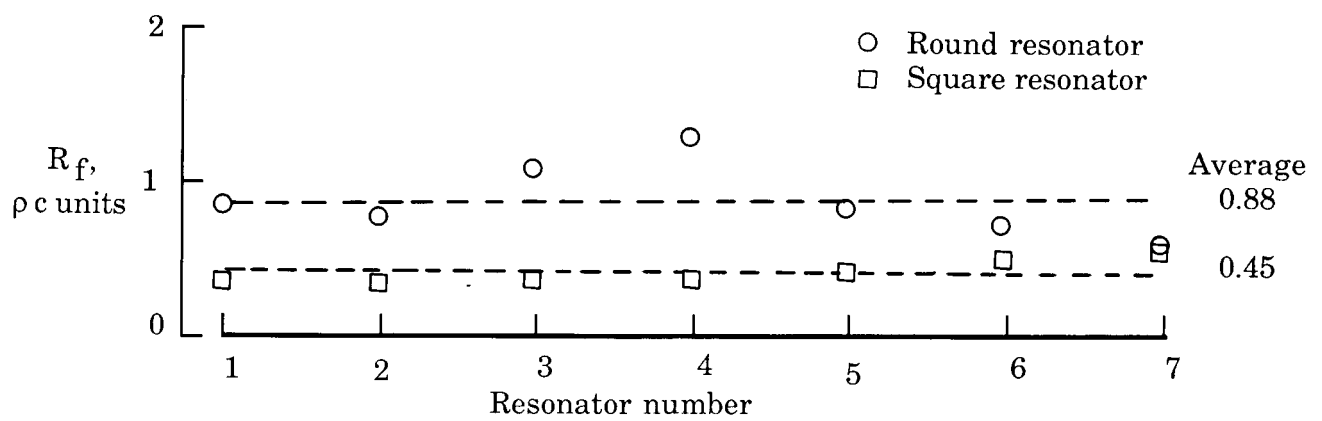
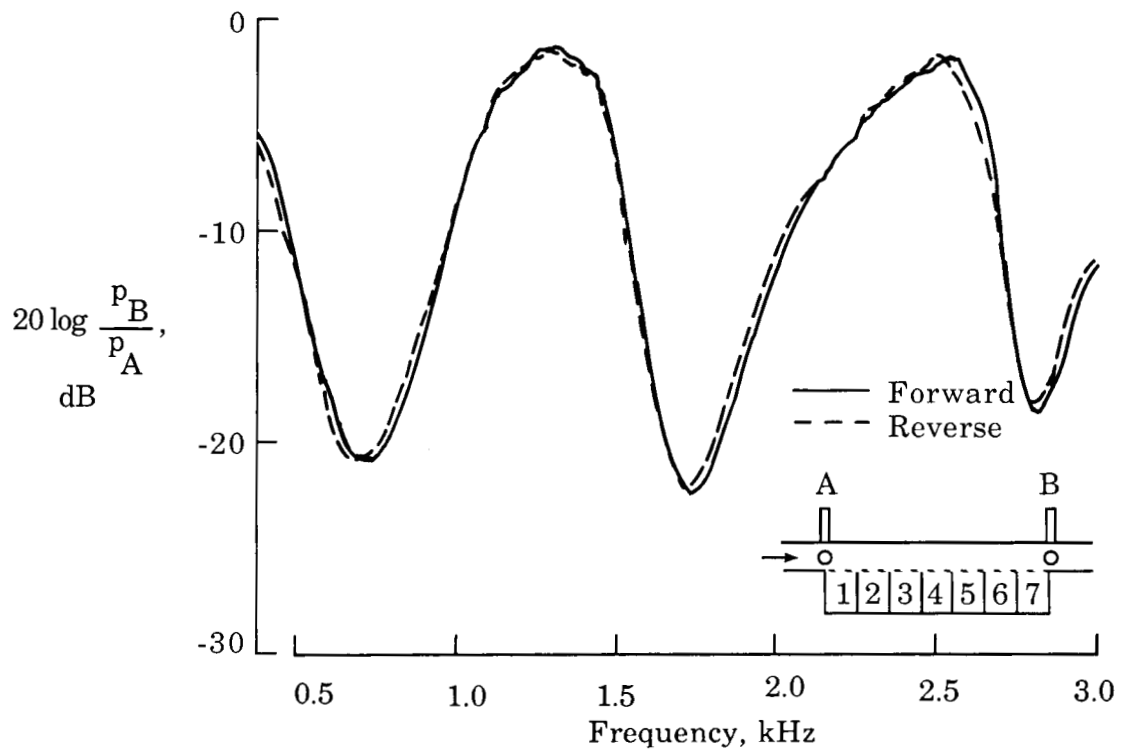
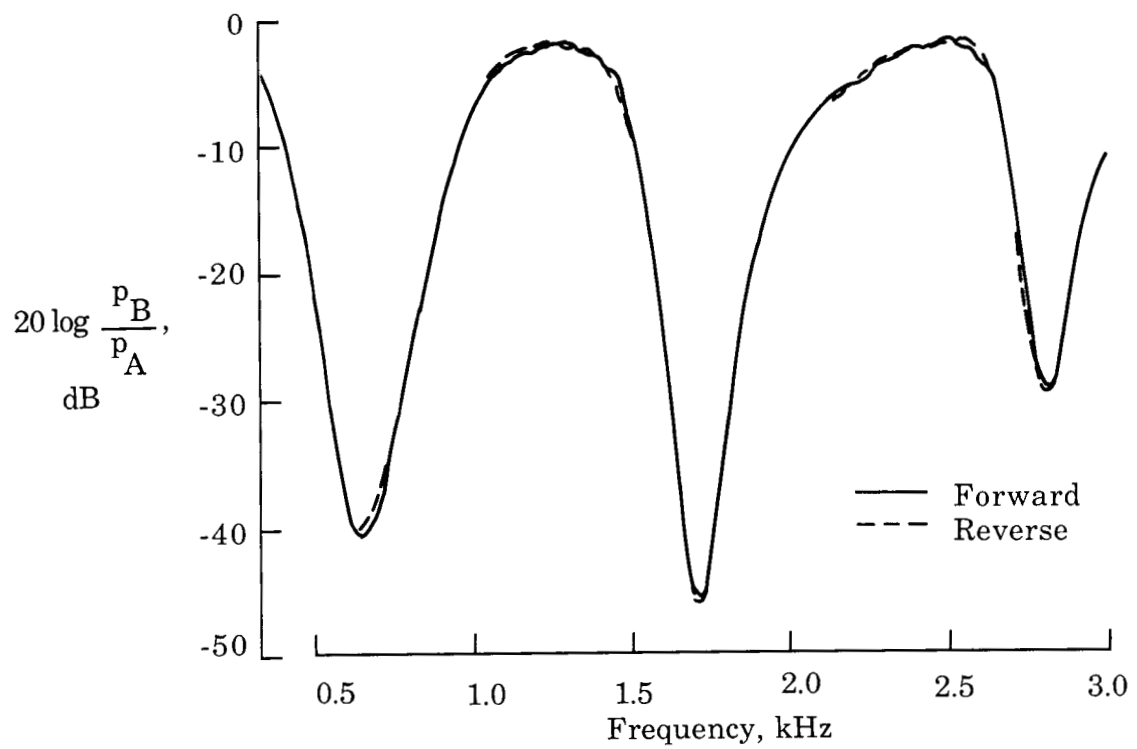


Figure 14. Flow resistance measurements of resonator array elements extrapolated to zero incident particle velocity.

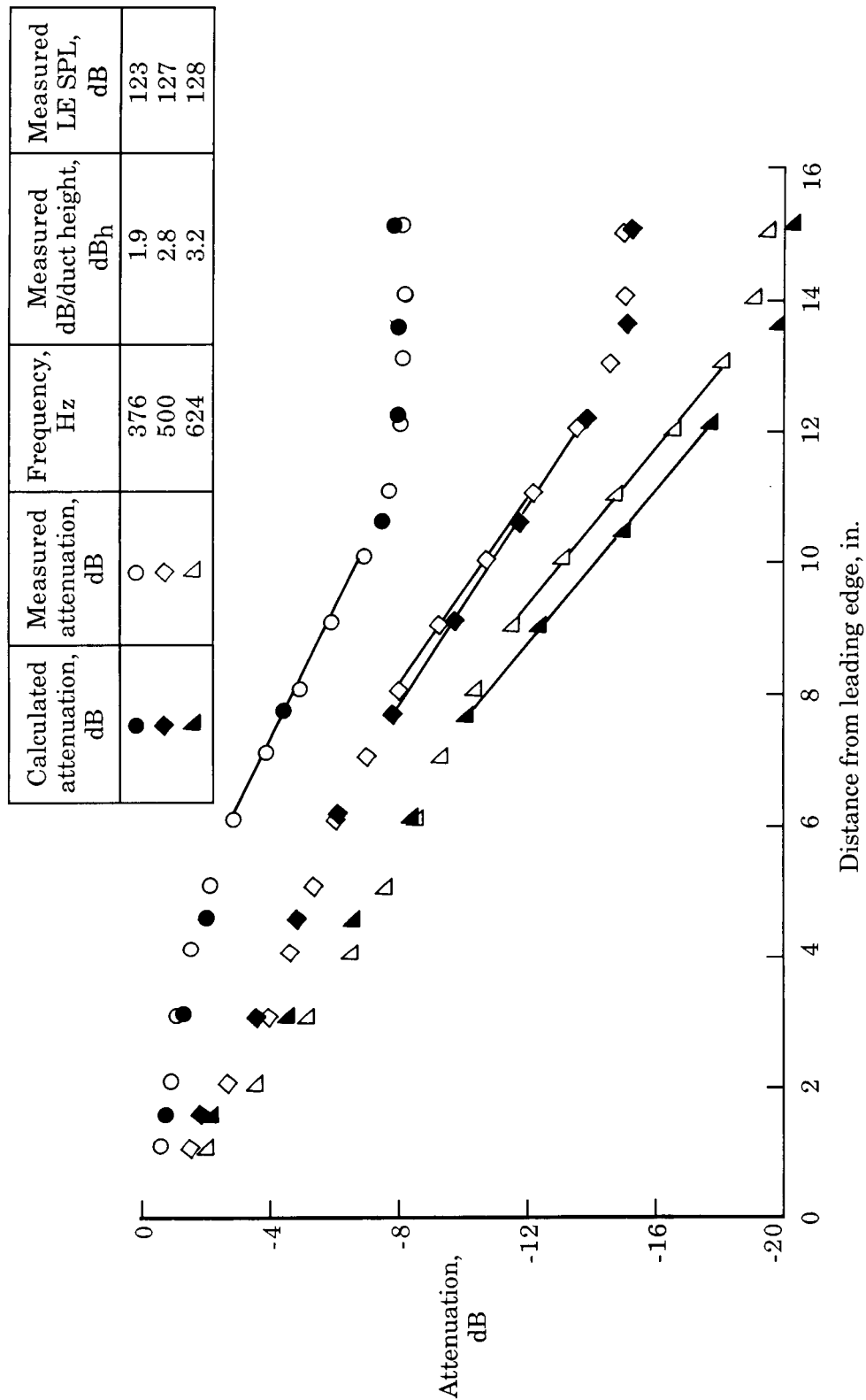


(a) Round resonator array.



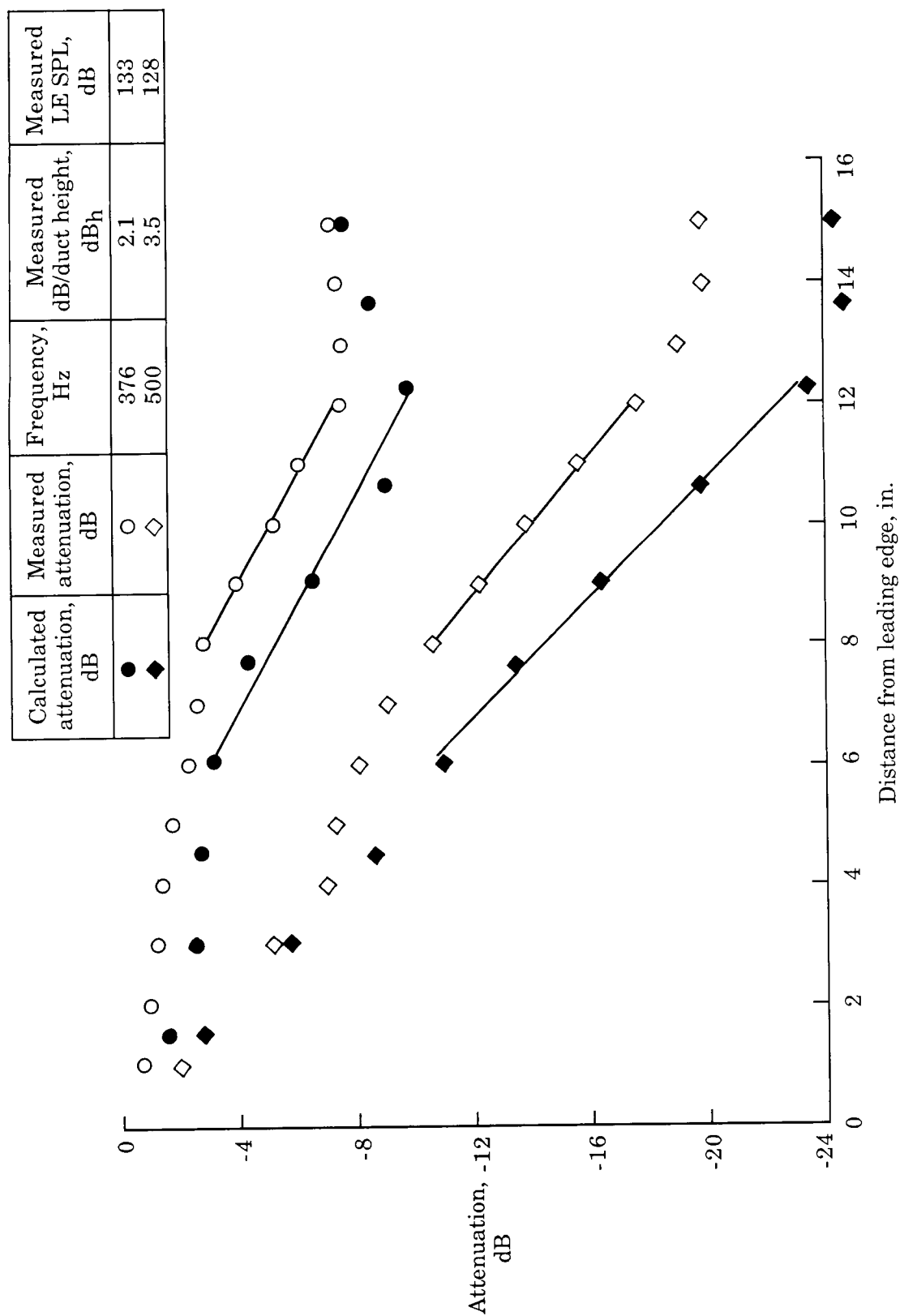
(b) Square resonator array.

Figure 15. Attenuation of broadband noise across resonator arrays for two different array orientations.



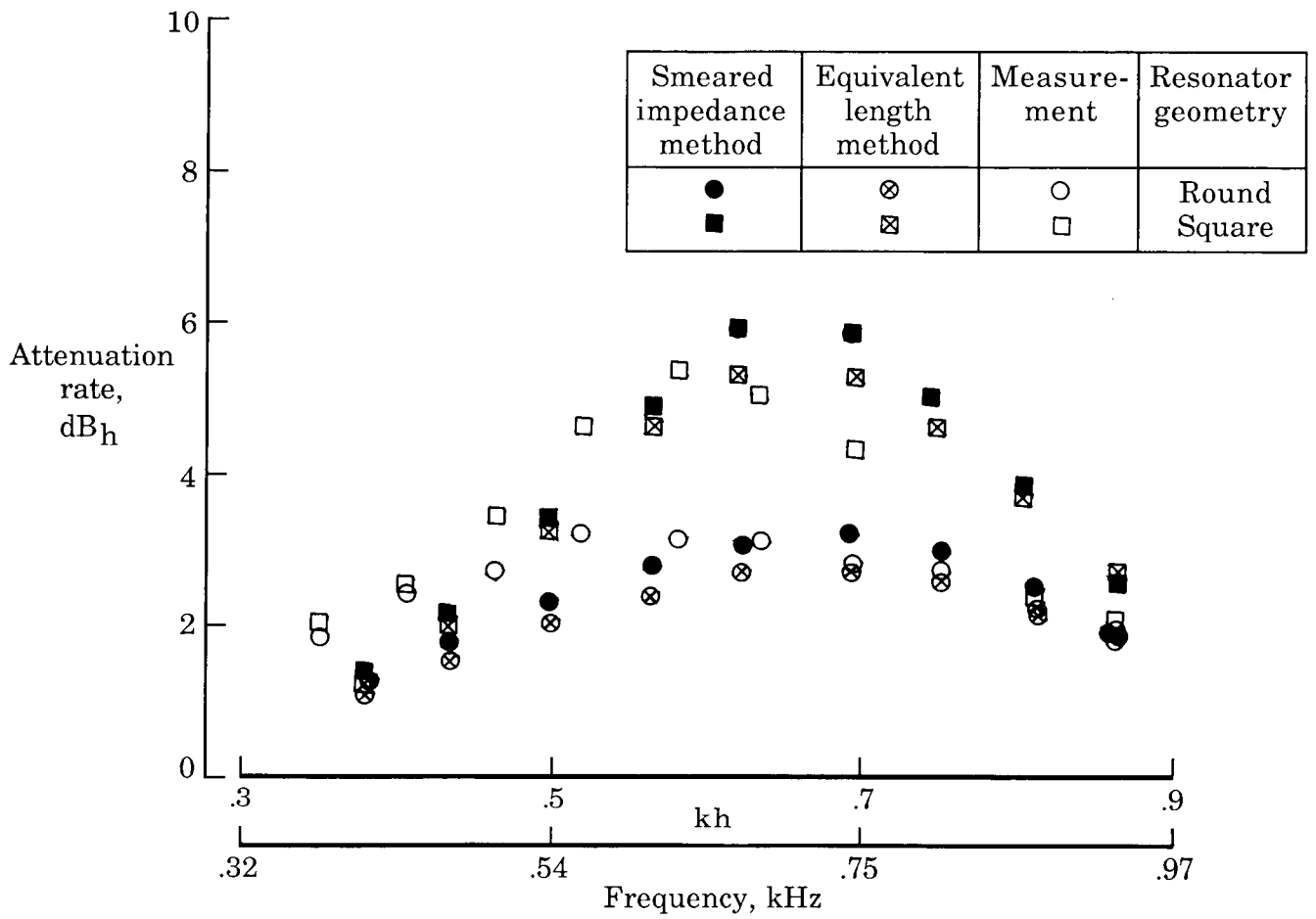
(a) Round resonator array.

Figure 16. Measured and calculated attenuation profiles (referenced to LE) for selected frequencies. Calculations were from finite element analysis method.



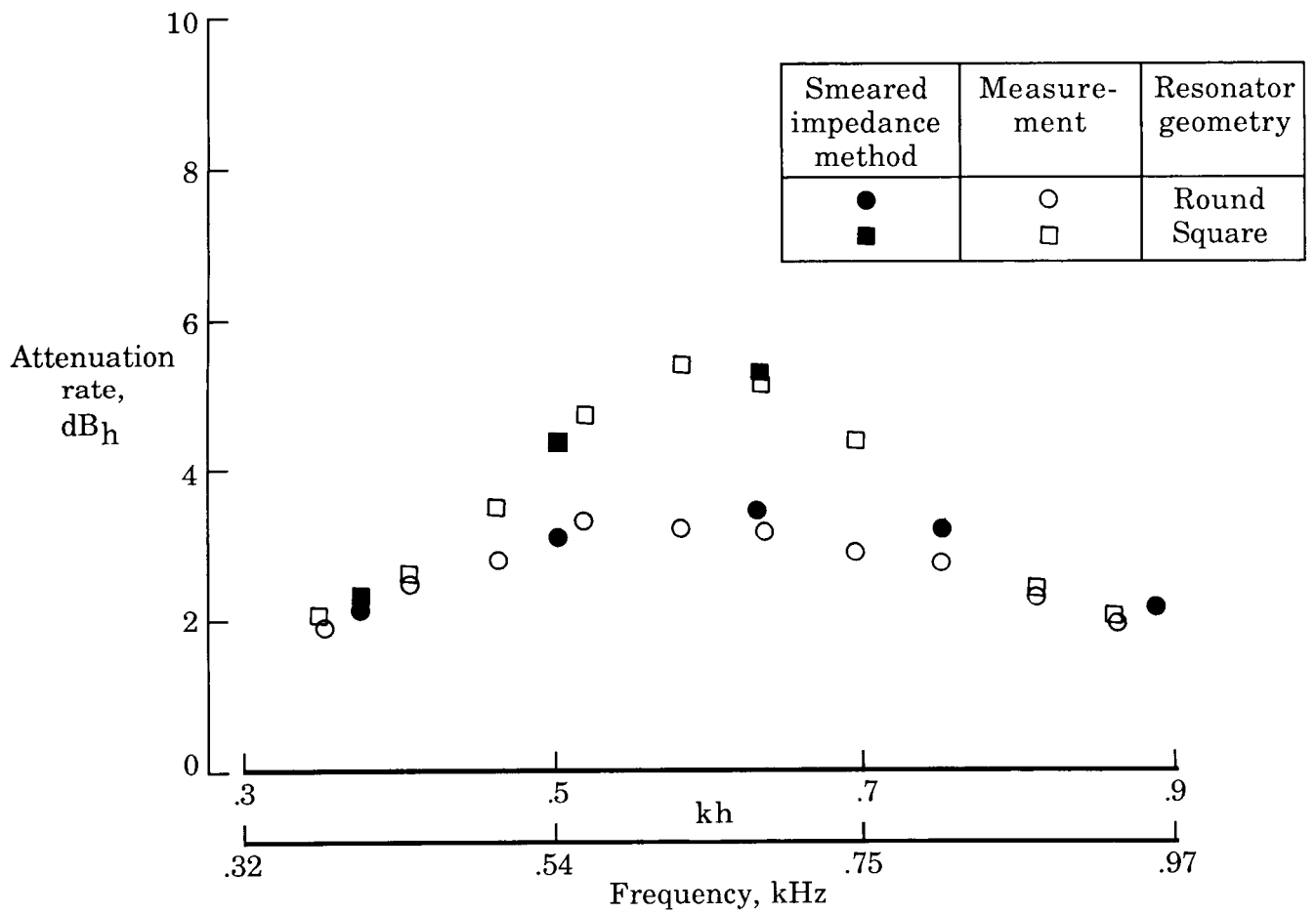
(b) Square resonator array.

Figure 16. Concluded.



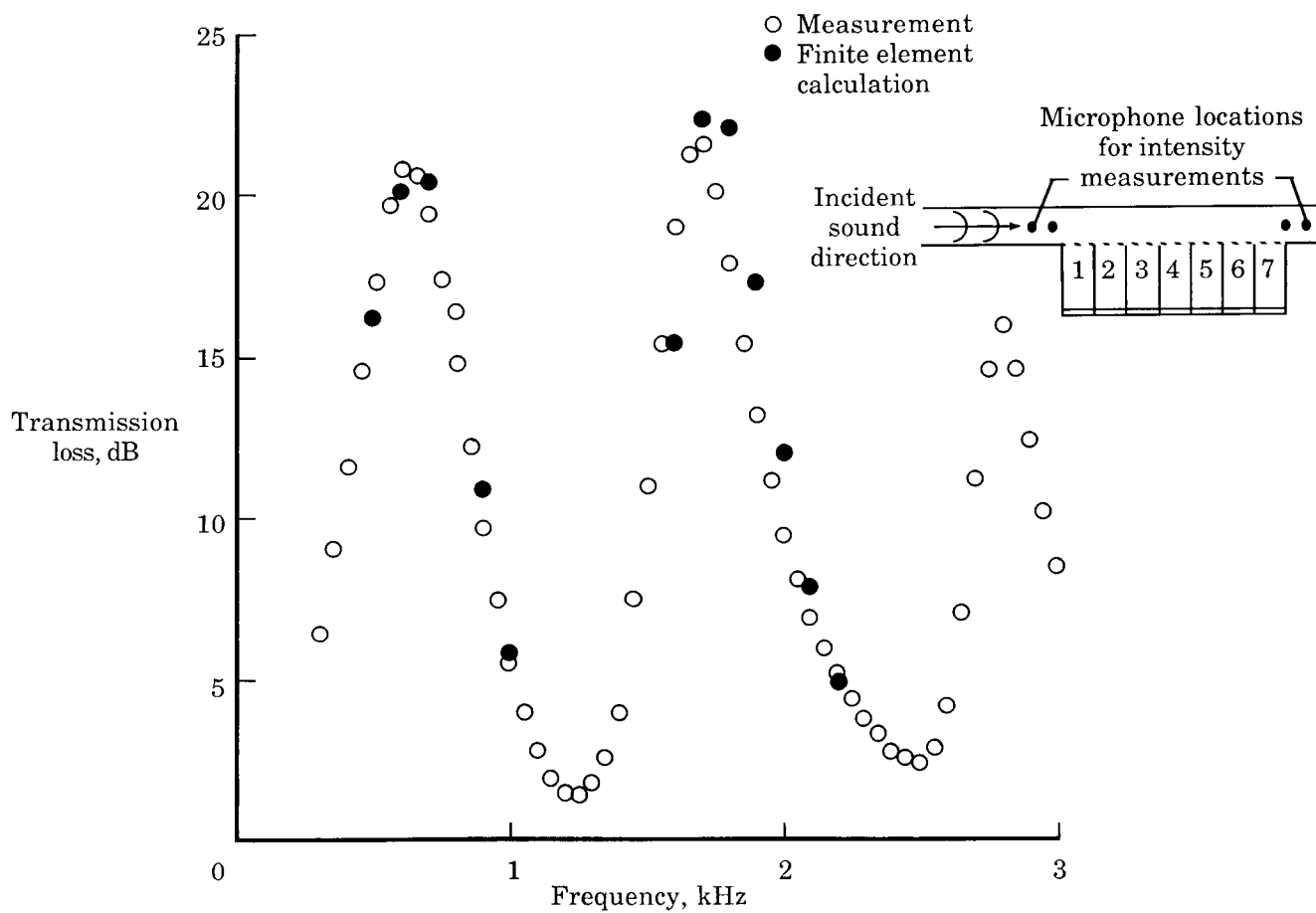
(a) Modal analysis method.

Figure 17. Measured and calculated attenuation rates.



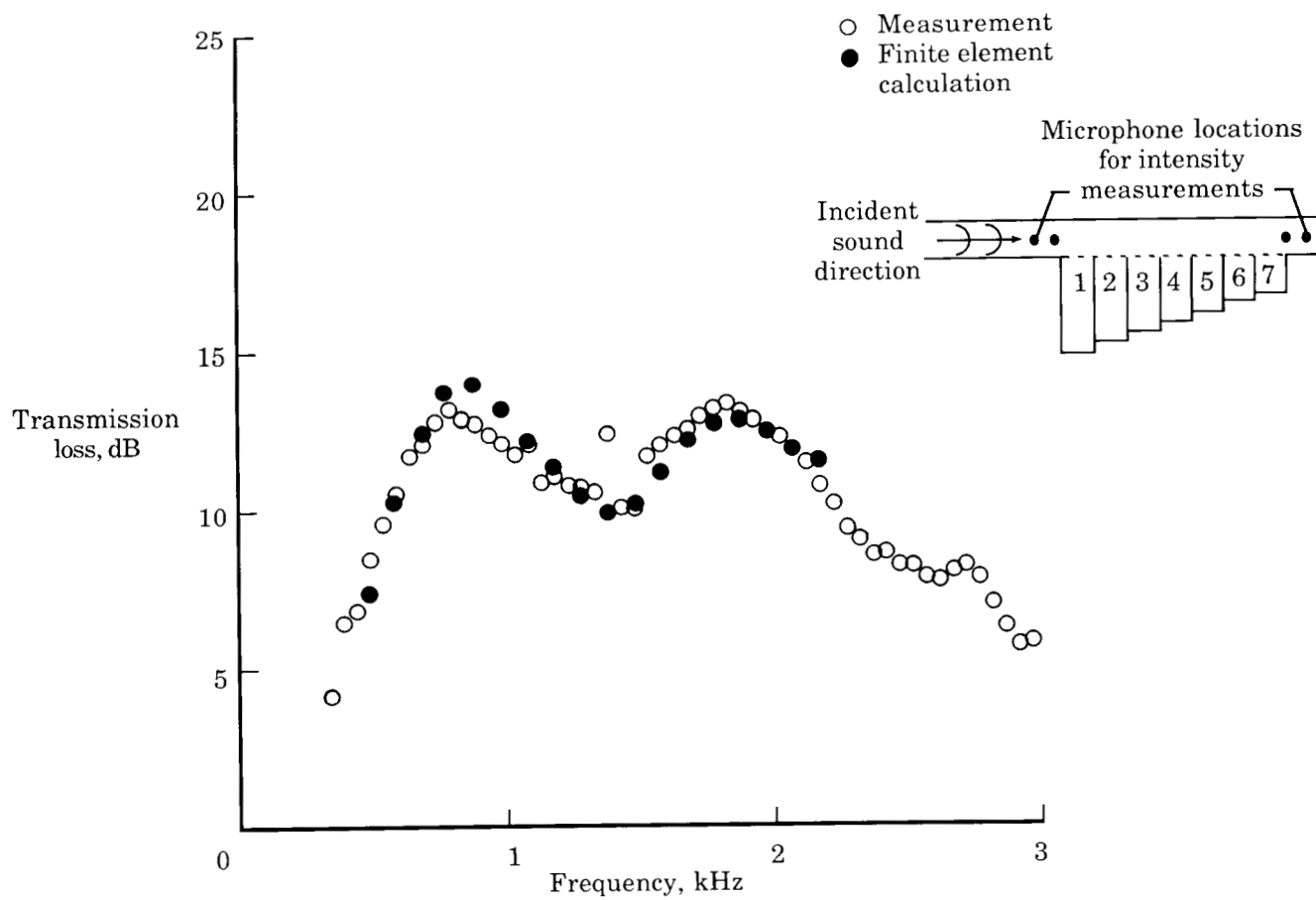
(b) Finite element analysis method.

Figure 17. Concluded.



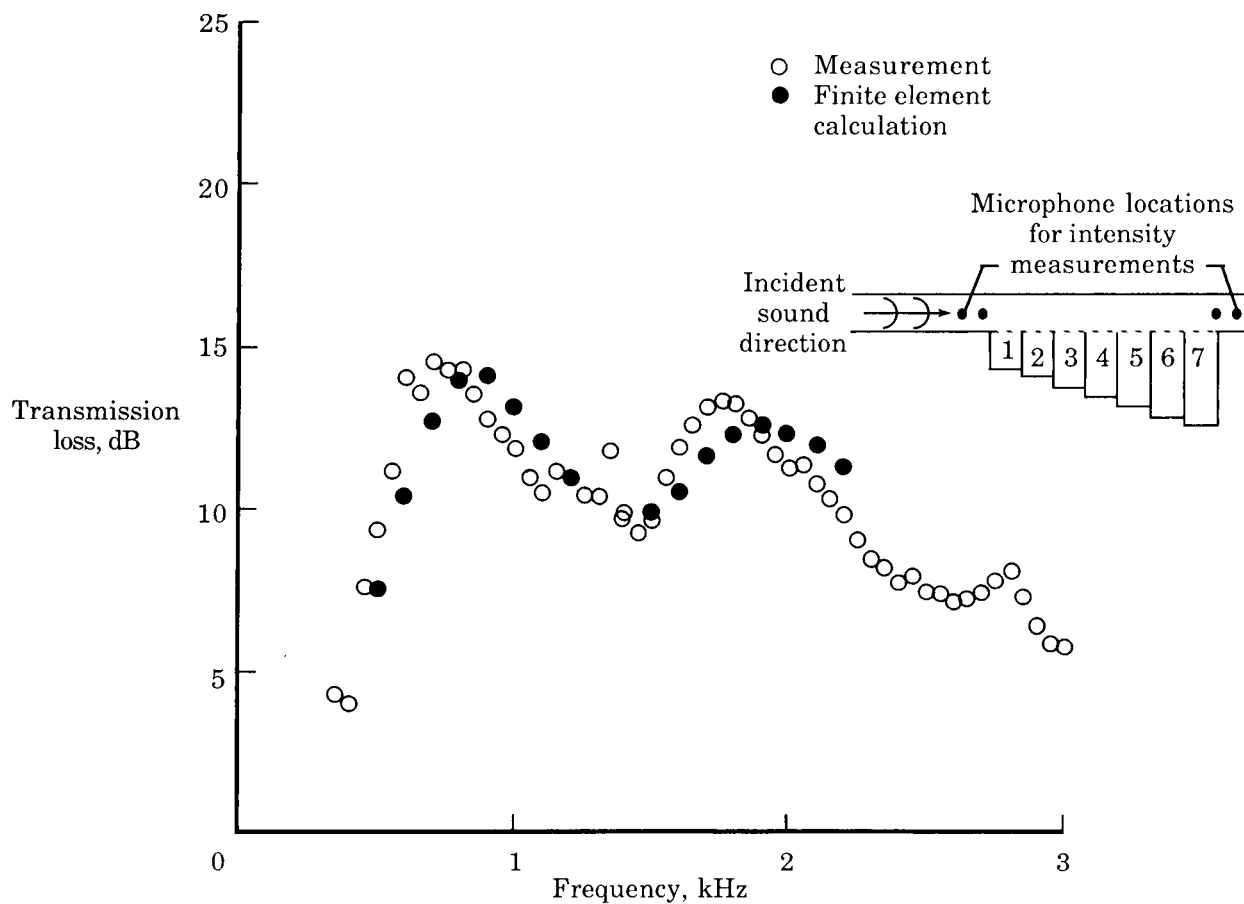
(a) Uniform cavity depths.

Figure 18. Measured and calculated transmission losses for round resonator array.



(b) Linear cavity depth variation, positive slope in propagation direction.

Figure 18. Continued.



(c) Linear cavity depth variation, negative slope in propagation direction.

Figure 18. Concluded.

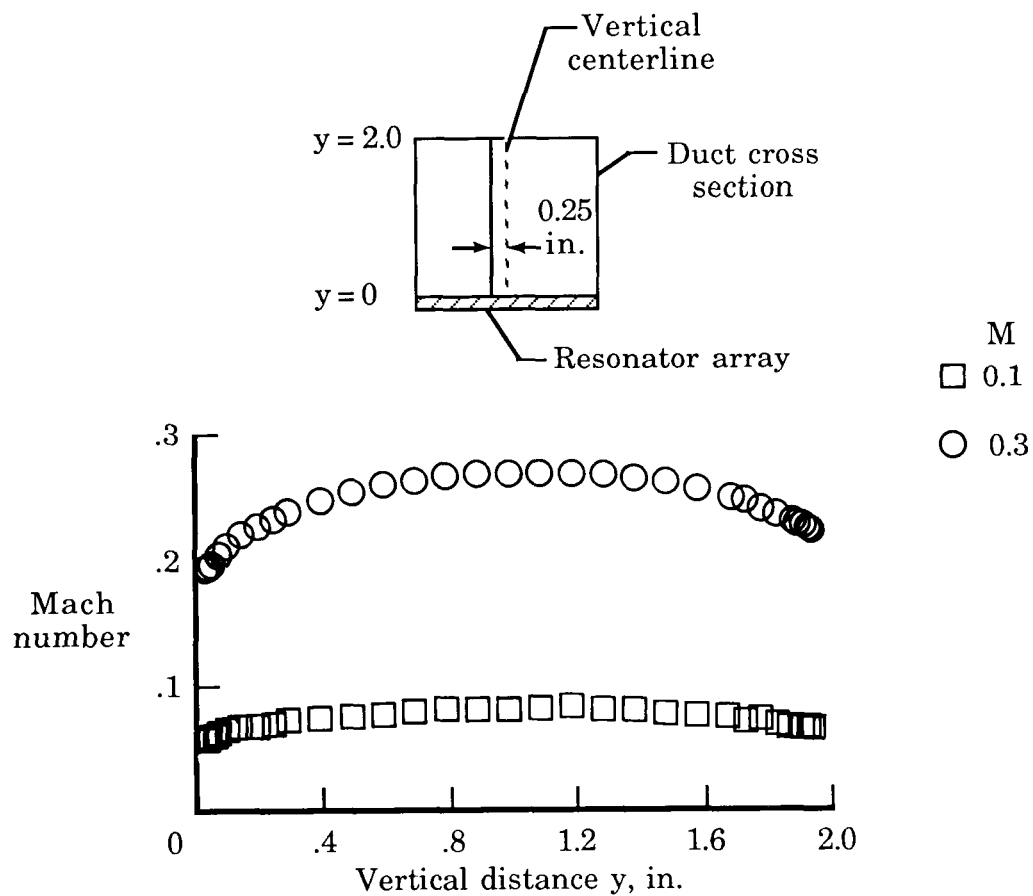


Figure 19. Vertical velocity profiles 0.25 in. from vertical centerline of test section for two centerline Mach numbers.

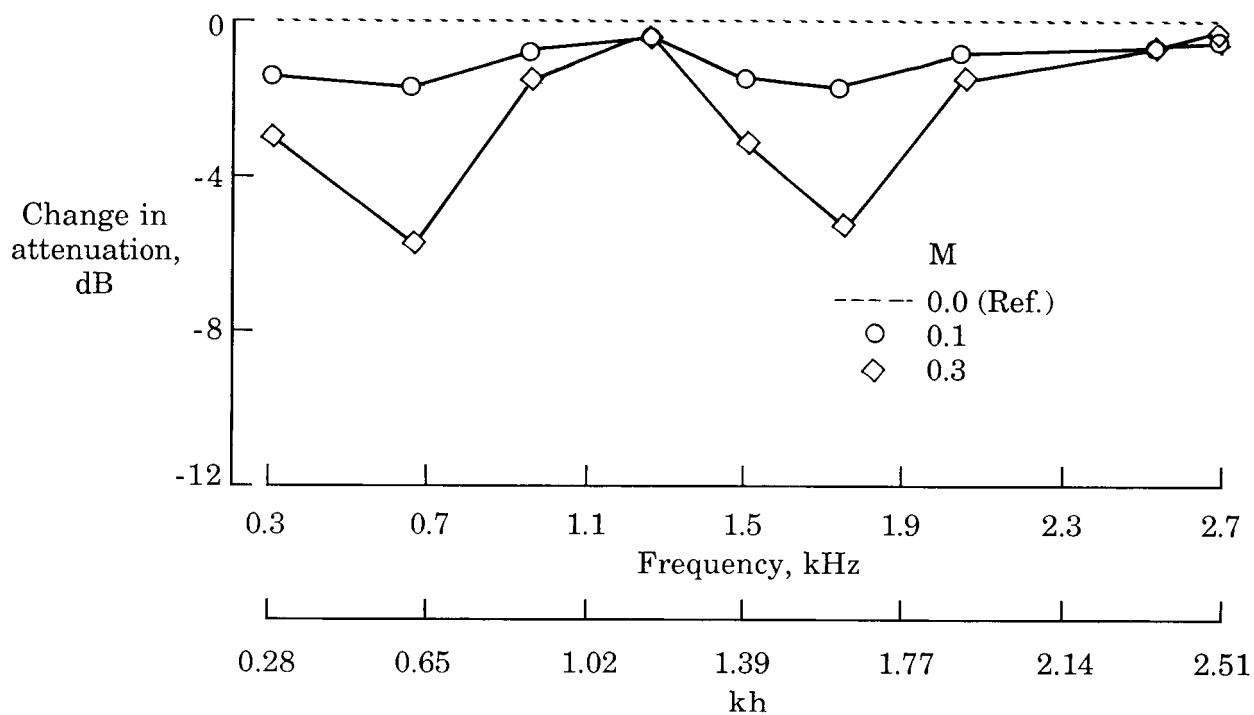


Figure 20. Change in attenuation because of mean flow for round resonator array.

ORIGINAL PAGE
COLOR PHOTOGRAPH

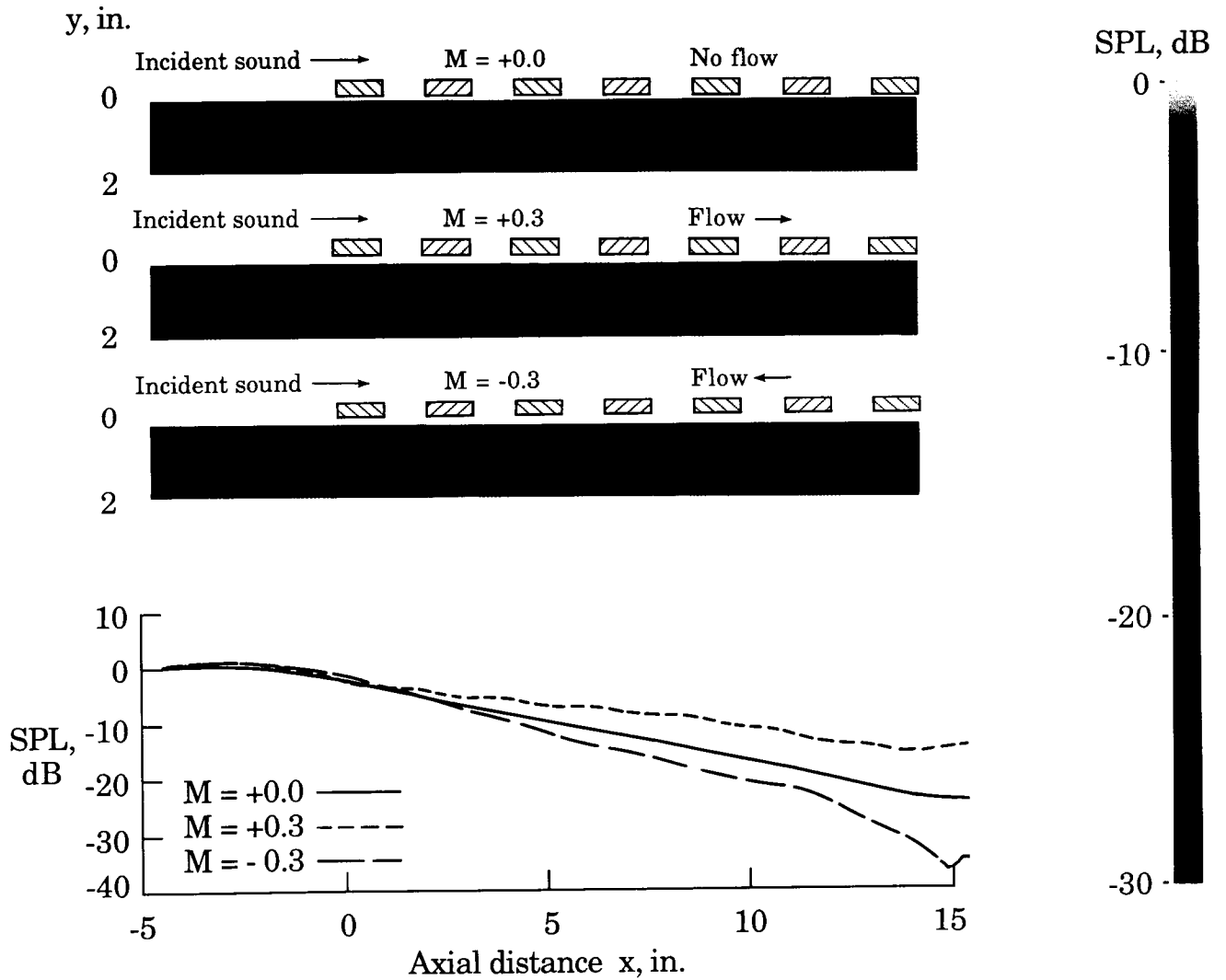
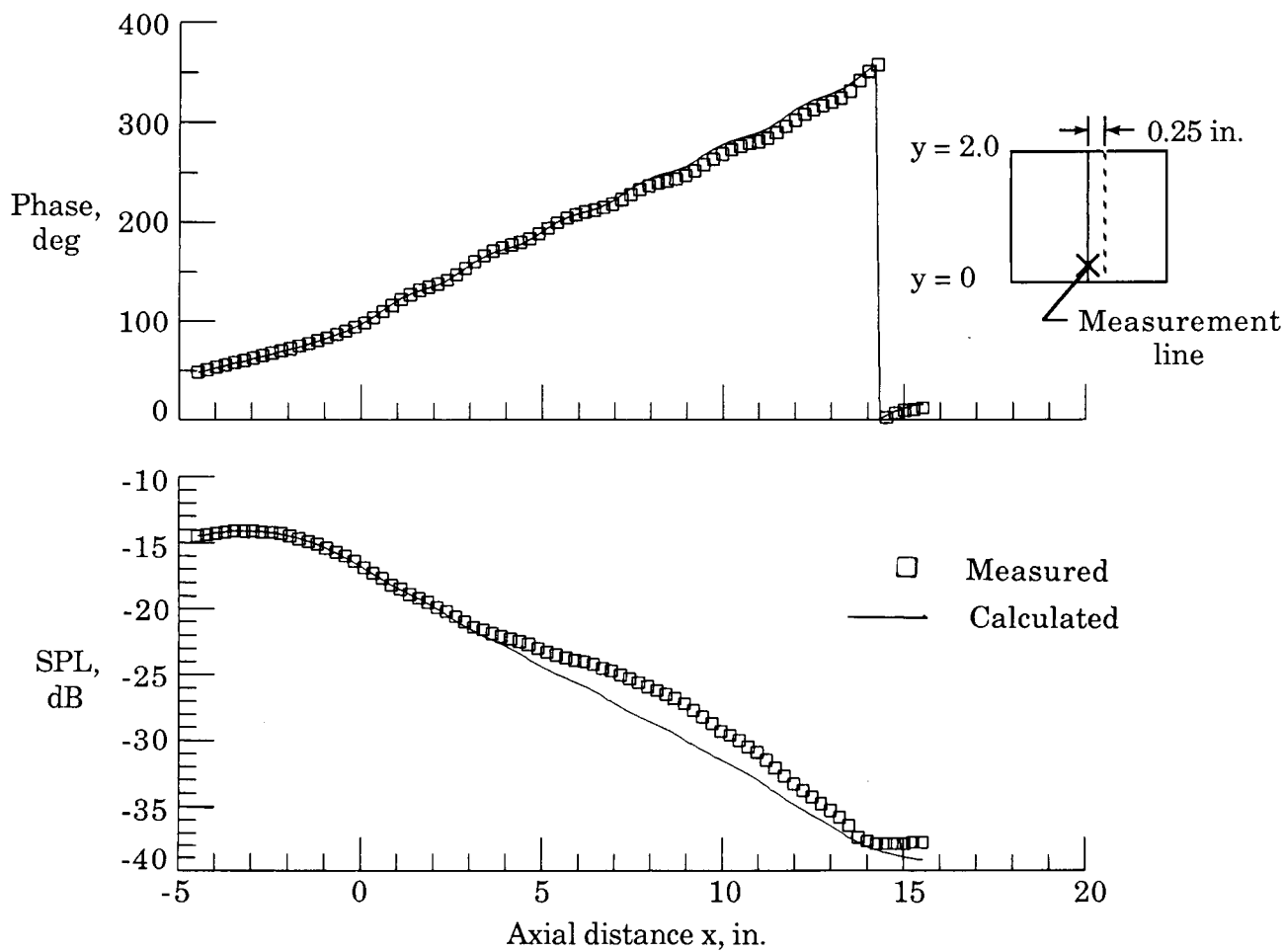
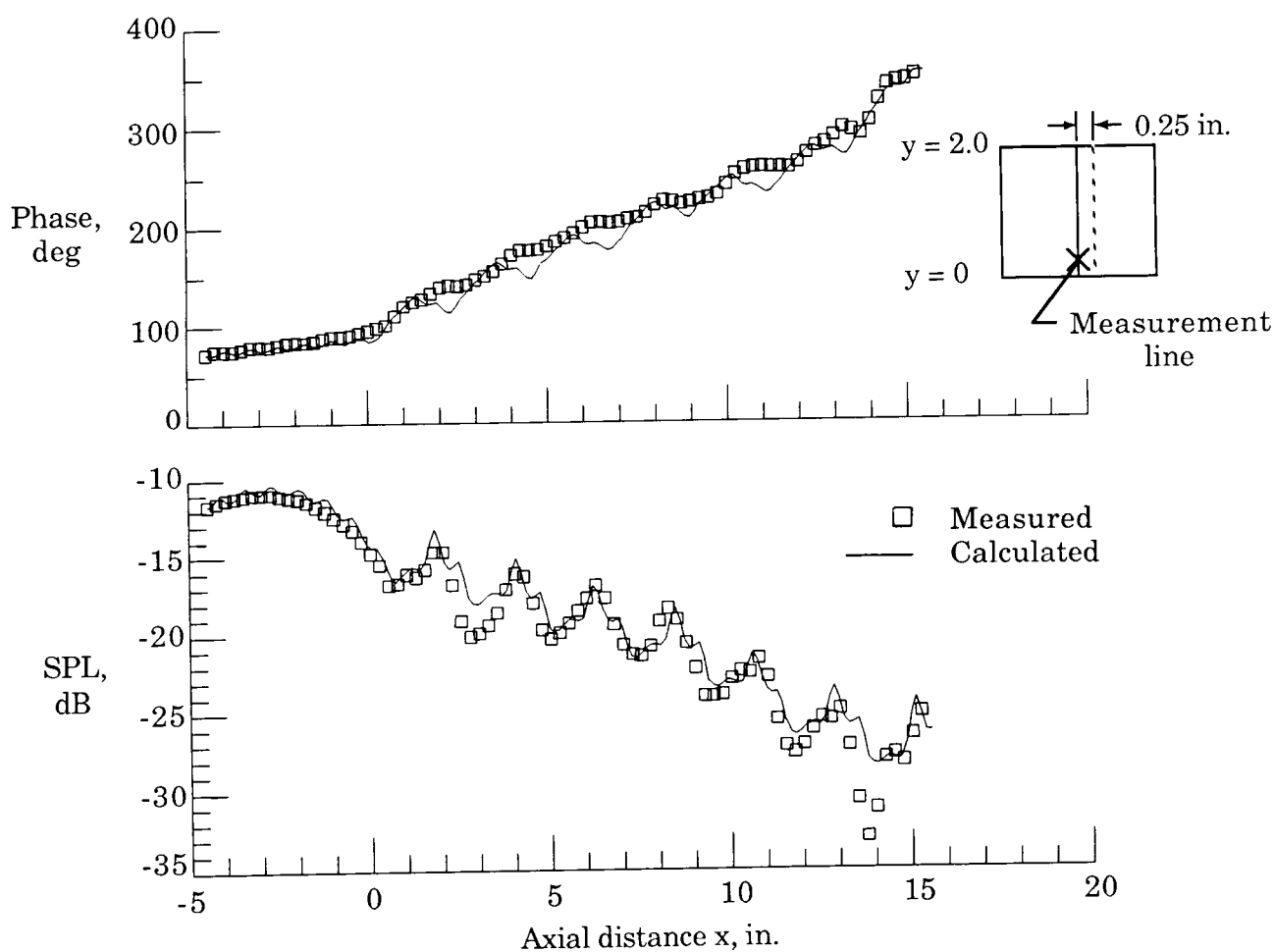


Figure 21. Calculated two-dimensional attenuation contours and centerline axial attenuations, relative to leading edge, for different mean flows at a frequency of 624 Hz.



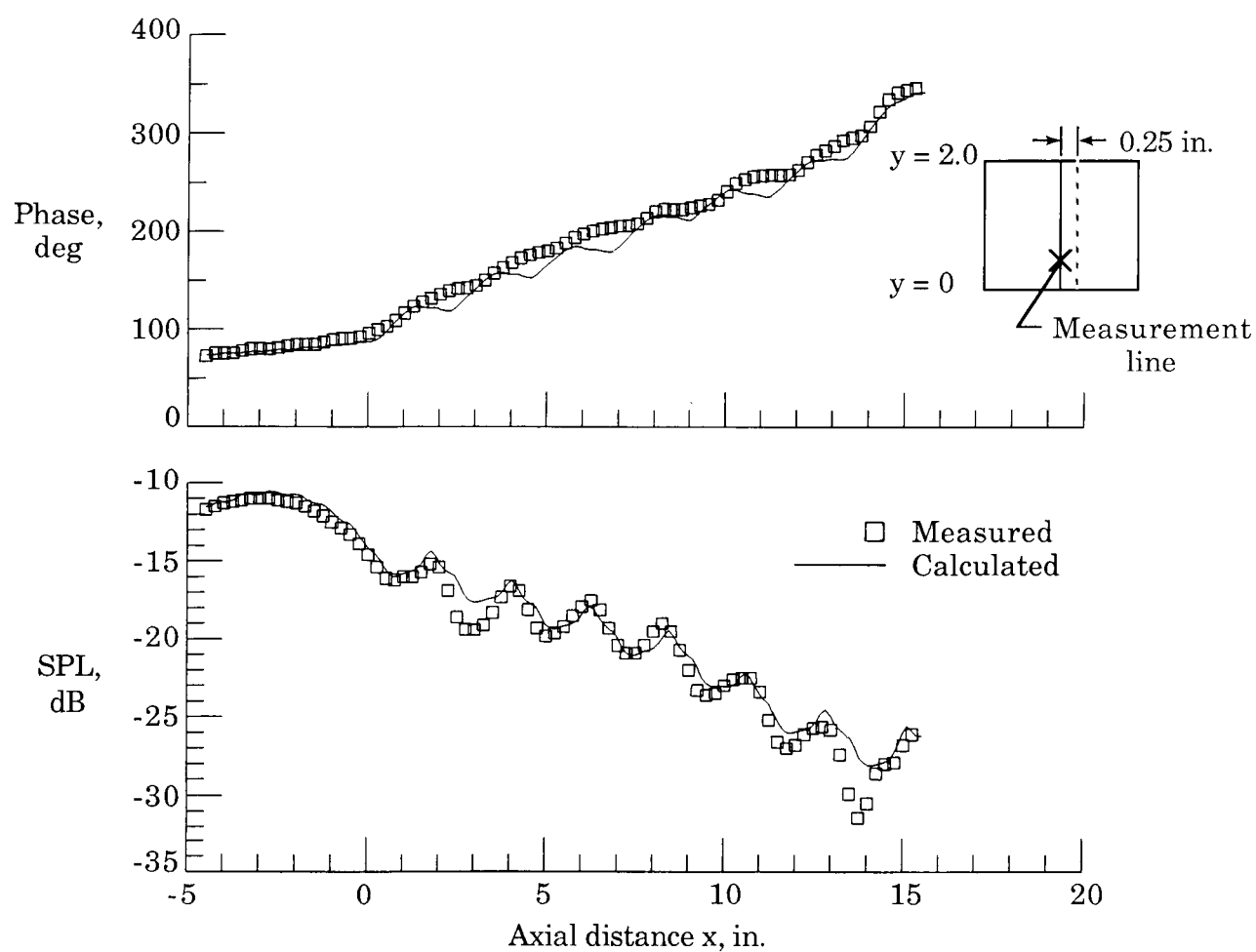
(a) $M = 0.0$, $y = 0.19$ in.

Figure 22. Measured and calculated flow effects on attenuation at various distances from round resonator array surface frequency 624 Hz.



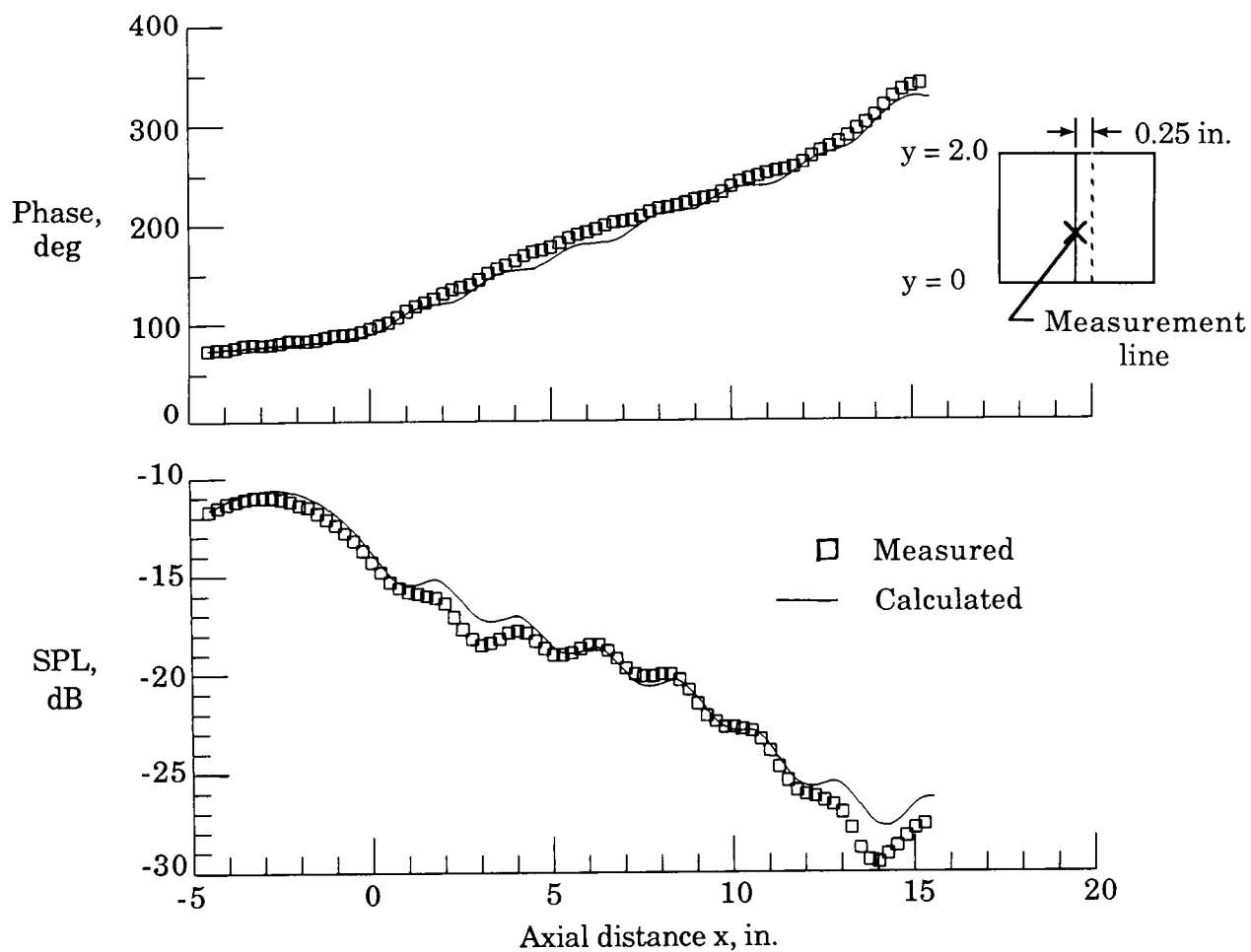
(b) $M = 0.3$, $y = 0.19$ in.

Figure 22. Continued.



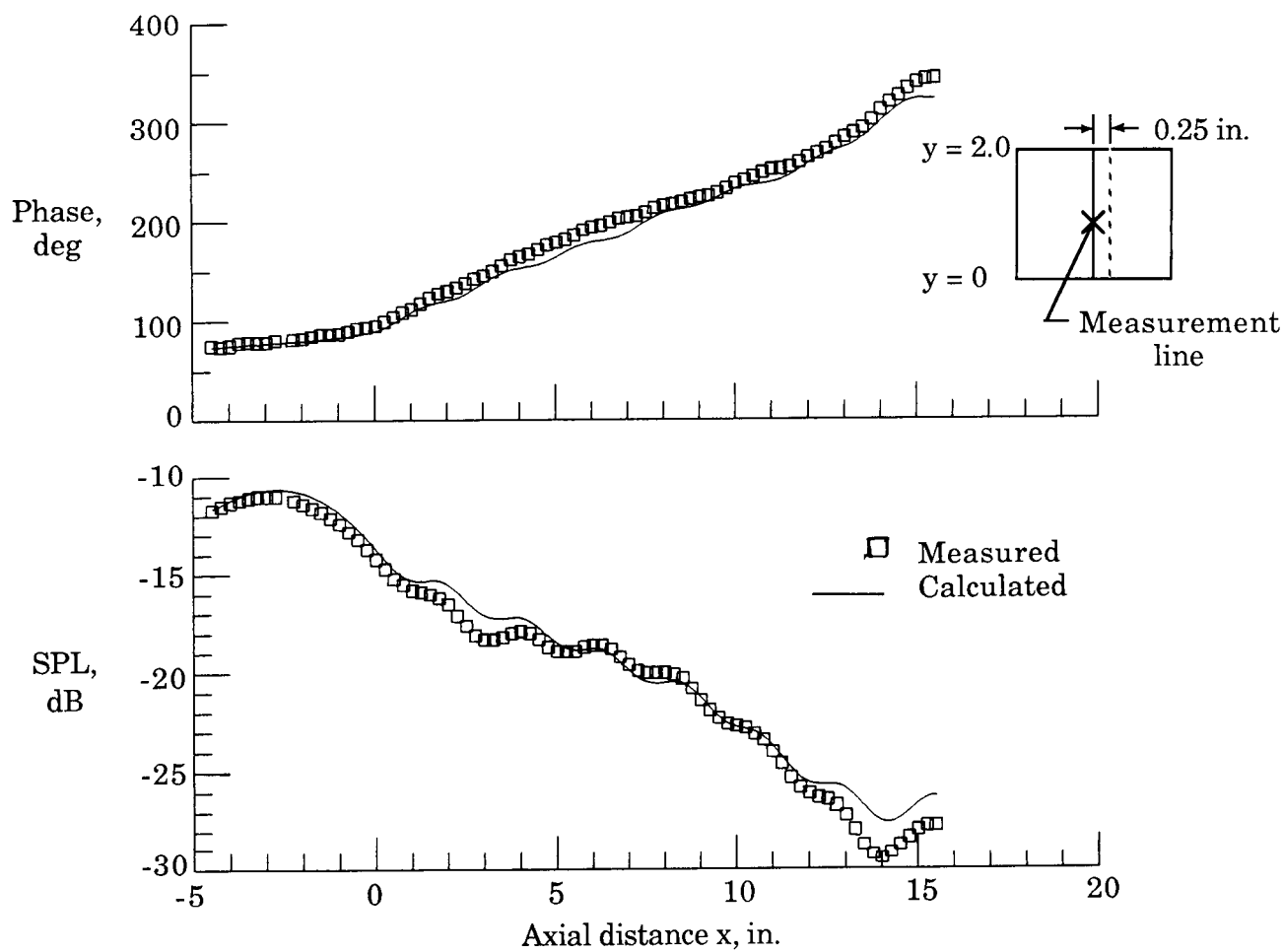
(c) $M = 0.3$, $y = 0.32$ in.

Figure 22. Continued.



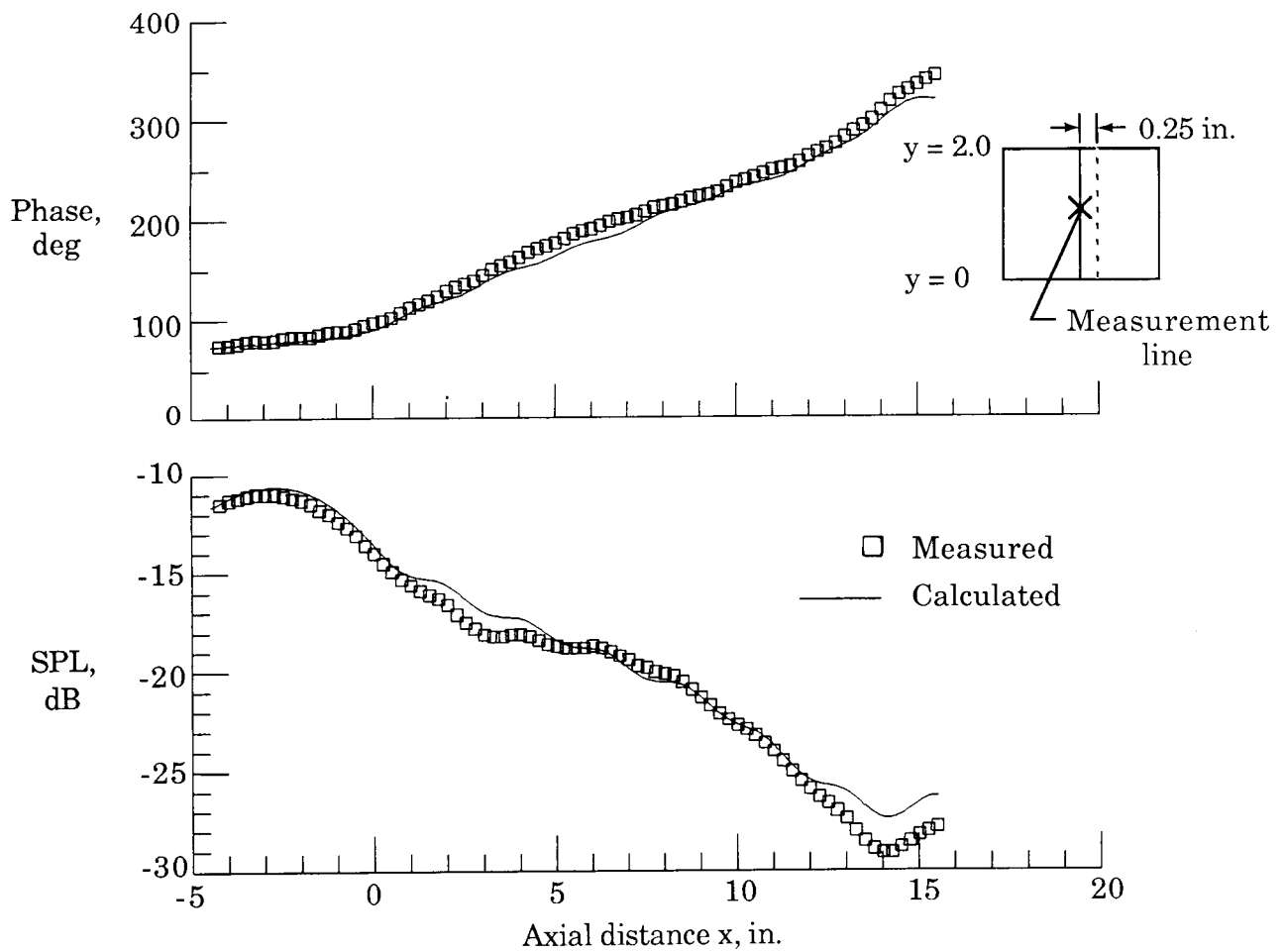
(d) $M = 0.3$, $y = 0.68$ in.

Figure 22. Continued.



(e) $M = 0.3$, $y = 0.81$ in.

Figure 22. Continued.



(f) $M = 0.3$, $y = 1.06$ in.

Figure 22. Concluded.

Report Documentation Page

1. Report No. NASA TP-2766		2. Government Accession No.		3. Recipient's Catalog No.	
4. Title and Subtitle Measured and Calculated Acoustic Attenuation Rates of Tuned Resonator Arrays for Two Surface Impedance Distribution Models With Flow				5. Report Date January 1988	
				6. Performing Organization Code	
7. Author(s) Tony L. Parrott, A. Louis Abrahamson, and Michael G. Jones				8. Performing Organization Report No. L-16352	
9. Performing Organization Name and Address NASA Langley Research Center Hampton, VA 23665-5225				10. Work Unit No. 505-61-11-02	
				11. Contract or Grant No.	
12. Sponsoring Agency Name and Address National Aeronautics and Space Administration Washington, DC 20546-0001				13. Type of Report and Period Covered Technical Paper	
				14. Sponsoring Agency Code	
15. Supplementary Notes Tony L. Parrott: Langley Research Center, Hampton, Virginia. A. Louis Abrahamson: COMTEK, Grafton, Virginia; work supported under NASA contract monitored by Dr. Lucio Maestrello. Michael G. Jones: PRC Kentron, Hampton, Virginia.					
16. Abstract An experiment was performed to validate two analytical models for predicting low-frequency attenuation of duct liner configurations built from an array of seven resonators that could be individually tuned by means of adjustable cavity depths. These analytical models had previously been developed for high frequency attenuation in aero-engine inlets. In the low frequency application, the linear surface impedance distribution is unavoidably spatially varying because of available fabrication techniques. The scale of this spatial variation may be a significant fraction of the acoustic wavelength. Measured and predicted attenuation rates and transmission losses for the modal decomposition and finite element propagation models were in good to excellent agreement for a test frequency range that included the first and second cavity resonance frequencies. This was true for both two surface impedance distribution modeling procedures used to simplify the impedance boundary conditions. With mean flow, measurements and calculations showed a fine-scale structure of acoustic "hot spots" in the attenuation and phase profiles. Since no impedance changes due to mean flow were assumed, it was concluded that this fine-scale structure was due to convective effects of the mean flow interacting with the surface impedance nonuniformities.					
17. Key Words (Suggested by Authors(s)) Resonator array Low-frequency noise attenuation Finite element model Modal decomposition model Impedance distribution				18. Distribution Statement Unclassified—Unlimited Subject Category 71	
19. Security Classif.(of this report) Unclassified		20. Security Classif.(of this page) Unclassified		21. No. of Pages 49	
				22. Price A03	